REPORT DOCUMENTATION PAGE

Form Approved OMB NO. 0704-0188

1. REPORT DATE (DD-MM-YYYY)
21-01-2017

2. REPORT TYPE
Final Report

3. DATES COVERED (From - To)
1-Oct-2010 - 30-Sep-2014

4. TITLE AND SUBTITLE
Final Report: Bio-Inspired Methods for Producing Adaptive Beampatterns with Diffracting Baffle Shapes

5a. CONTRACT NUMBER
W911NF-10-1-0527

5b. GRANT NUMBER

5c. PROGRAM ELEMENT NUMBER
611102

5d. PROJECT NUMBER

5e. TASK NUMBER

5f. WORK UNIT NUMBER

6. AUTHORS
Rolf Mueller

7. PERFORMING ORGANIZATION NAMES AND ADDRESSES
Virginia Polytechnic Institute & State Unive
North End Center, Suite 4200
300 Turner Street, NW
Blacksburg, VA 24061 -0001

8. PERFORMING ORGANIZATION REPORT NUMBER

9. SPONSORING/MONITORING AGENCY NAME(S) AND ADDRESS (ES)
U.S. Army Research Office
P.O. Box 12211
Research Triangle Park, NC 27709-2211

10. SPONSOR/MONITOR'S ACRONYM(S)
ARO

11. SPONSOR/MONITOR'S REPORT NUMBER(S)
57005-NS.41

12. DISTRIBUTION AVAILIBILITY STATEMENT
Approved for Public Release; Distribution Unlimited

13. SUPPLEMENTARY NOTES
The views, opinions and/or findings contained in this report are those of the author(s) and should not contrued as an official Department of the Army position, policy or decision, unless so designated by other documentation.

14. ABSTRACT
The diversity of local shape features and their role in shaping the functional/ultrasonic characteristics of the noseleaves and pinnae in bats have been investigated. Using smoothing and other shape manipulation techniques, local features were changed and their acoustic impact observed. It was found that several local features of the noseleaves and pinna did have strong and consistent impacts on the

15. SUBJECT TERMS
bioinspired sensing

16. SECURITY CLASSIFICATION OF:

a. REPORT	b. ABSTRACT	c. THIS PAGE
UU	UU	UU

17. LIMITATION OF ABSTRACT
UU

15. NUMBER OF PAGES

19a. NAME OF RESPONSIBLE PERSON
Rolf Mueller

19b. TELEPHONE NUMBER
540-231-6005

Standard Form 298 (Rev 8/98)
Prescribed by ANSI Std. Z39.18

RPPR
as of 17-Apr-2018

Agency Code:

Proposal Number:

Agreement Number:

Organization:
Address: , ,
Country:
DUNS Number:
EIN:
Report Date:
Date Received:
for Period Beginning and Ending
Title:
Begin Performance Period:
End Performance Period:
Report Term: -
Submitted By:
Email:
Phone:
Distribution Statement: -

STEM Degrees:

STEM Participants:

Major Goals:

Accomplishments:

Training Opportunities:

Results Dissemination:

Plans Next Period:

Honors and Awards:

Protocol Activity Status:

Technology Transfer:

1 Foreword

The diversity of local shape features and their role in shaping the functional/ultrasonic characteristics of the noseleaves and pinnae in bats have been investigated. Using smoothing and other shape manipulation techniques, local features were changed and their acoustic impact observed. It was found that several local features of the noseleaves and pinna did have strong and consistent impacts on the beampatterns. Computer animations techniques have been used to recreate active deformations of the noseleaf shapes that some bat species show as part of their biosonar behaviors and put the resulting changes to the shapes and their acoustic characteristics into the context of the interspecific variability. Significant progress has been made towards analyzing the variability in the variability in the noseleaf shapes and in the beampatterns. For the noseleaf shapes, two approaches have been pursued. In particular, an approach based on morphing of canonical shape models has shown promising results with respect to retaining three-dimensional features of the noseleaves and a first set of eigenvectors has already been obtained. A solution to the beampattern alignment problem based on p-norm cost functions and a limited search space has been devised and tested on representative beampattern sample.

Contents

List of Figures

2 Statement of the Problem Studied

The biosonar system of bats is a highly capable active biological sense that allows the animals to thrive in structure-rich natural environments that still pose insurmountable problems to engineered sensing systems. At the same time, bat biosonar is extremely diverse with around 1000 biological species that use sonar to live in diverse habitats and pursue a wide range of different prey. The research reported here was aimed at characterizing the diversity and complexity in the device characteristics of the bat biosonar systems and the mechanical structures ("noseleaves" and outer ears) that produce them.

3 Data Set Preparation

The goal of the data set preparation was to maximize the quantity and quality of the geometry of beamforming baffle shapes represented in the analysis. An initial set of shape data with about 1,000 digitized shapes of bat pinnae and noseleaves was available as raw material for the selection of the data set to be used in the project. However, the shapes in the raw data set differed significantly in quality with respect to the presence of *post-mortem* artifacts in the shapes. Hence, all shapes in the were checked for the presence of artifacts when considering them for inclusion the project data set. Besides the quality of the included shapes, selection was also guided by the principle of establishing a balanced data set to cover as much of the natural diversity in these biological beamforming structures as possible without being biased towards any taxonomic group. It was also attempted to balance emission beamforming shapes (i.e., noseleaves) with reception beamforming shapes (i.e., outer ears).

The final data set that has been compiled through a process that included vetting of each sample as well as balancing between noseleaves, outer ears, and different taxonomic groups contains 361 digital shape in total. Out of these, 176 shapes were noseleaves (s. Figure 1) and 185 shapes of outer ears (s. Figure 2). The shapes in the data set (s. Table 1) represent a total of 106 different bat species. This corresponds to about 10% of the total number of known bat species in the world [27].

During the process of compiling the shape data base for the current project, the samples were not only vetted for *post-mortem* artifacts, but the digital representations of the shapes were also improved. In particular, topological errors in the polygonal meshes that are used to describe the surfaces of the biological shapes were fixed in the process. The surfaces meshes were created from binary (i.e., black-and-white)

Figure 1: Renderings of the 176 noseleaf shapes included in the analysis data set.

Figure 2: Renderings of the 185 pinnae included in the analysis data set.

voxel representations that were in turn derived from stacks of computer tomographic cross-section images. This was done using the marching cubes algorithm [12] as implemented in the "Visualization Toolkit" library

(VTK, [24]). The number of polygons was reduced using the VTK's decimation algorithm [25]. However, it was discovered that the resulting meshes contained errors such as being non-manifold mesh (i.e., edges being shared between polygons) or surfaces being not closed. Such problems prohibit the use of the methods of quantitative shape analysis that are currently being tested for characterizing the biodiversity in the shape data set. Hence, the polygon meshes produced by VTK were post-processed to created closed meshes (using the software *Polymender* [11]) and remove small surface "handles" (e.g., artificial connections between neighboring parts) using the software *TopoMender* [28]. Finally, the number of polygons in the mesh was further reduced to around 100,000 triangles per sample using the software *QSlim* [6]. Together, all these processing steps insured that the digital representations for all 361 shapes in the database are accurate, free of topological errors, as well as ready for processing in an efficient manner.

4 Matching Shape Data with Beampattern Estimates

An extensive search of the biological literature has been conducted for each of the 106 species in the sample to determine the frequency bands that the biosonar pulses of each species have been reported to occupy. For a few species where no such information could be found in the literature, data from closely related species (i.e., sibling species from the same genus) was used. Furthermore, a few of the bat species in the sample are known not to use active sonar. However, these species were added to the data set as reference in case features that set an active biosonar system apart can be found. For these species, a frequency range was set based on the 90% percentiles of the frequency band distribution that was derived from the species with active biosonar in the sample. The 90% percentile frequency band extended from 20 to 125 kHz.

For all 361 shape samples in the data set, estimates of the emission or reception beampatterns have been obtained using numerical methods (s. Figures 9 to 19, 2 beampatterns are not shown because the calculations were rechecked at the time of writing). For each sample, numerical beampattern estimates were computed at ten frequencies that were spaced equally across the frequency band determined as described above. The employed numerical methods were previously developed custom tools that simulate the acoustic near-field in the immediate vicinity of the diffracting ear or noseleaf surfaces using a finite-element approach. These near-field results form the basis for a prediction of the far-field directivity pattern using a free-field projection based on a Kirchhoff Integral formulation. Beampatterns were predicted with a resolution of 1 degree in azimuth and in elevation.

The unprecedented size and diversity of the shape data set to which these numerical methods have been applied, has posed a challenge and several small issues in model preparation and setting up the iterative solvers have surfaced in the process. A final quality check for weeding out and rectifying single erroneous numerical predictions from the 361 simulations is still ongoing and is expected to be finished within two weeks of filing this report. At this point in time, this research project will have produced a data set on the shapes and acoustic properties of biological beamforming baffle shapes that exceeds any prior art not only in quantity by at least one order of magnitude, but also in accuracy, resolution, and the biodiversity covered.

5 Development of Methods for Data Analysis

In parallel with the compilation/creation of the experimental data set, work on the development of methods for analyzing the data set has commenced. This research work has focused on three aspects of the analysis to be undertaken:

1. shape characterization and manipulation,

2. beampattern characterization,
3. beampattern alignment across species.

The development of the methods for shape characterization and manipulation has benefited from a parallel collaborative research project on biological shape spaces (sponsored by NSF, PI: Rolf Mueller) in which tools for describing and manipulating biological shapes are developed.

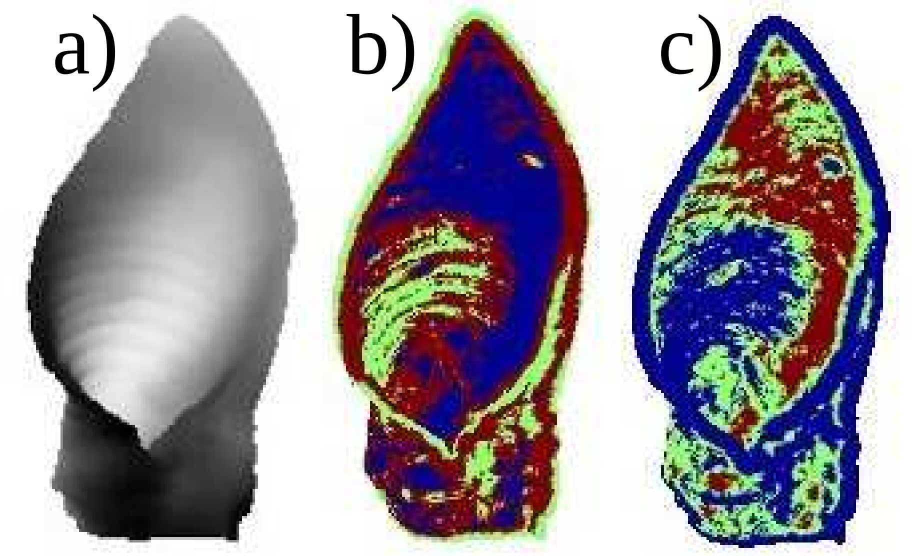

Figure 3: Example of alternative clustering methods applied to a local shape metric computed over an outer ear surface (a). In each alternative clustering (b,c), three different clusters were identified (coded by color). In this trial, the surface areas corresponding to the ear border and the area of the washboard ripple pattern were clustered together for both of the alternatives.

At present, local shape descriptors are being looked into as a way to characterize the shapes of the beamforming baffles in the data set. By themselves, these local shape descriptors will be used as tools to establish the presence or location of shape features such as ridges, grooves, flaps, and washboard ripple patterns on a given biological baffle. Furthermore, the results from applying the local shape metrics are currently being combined with advanced clustering methods so that they can be used to segment the biological baffle shapes into pieces and establish shape-based matches between features across baffle shapes from different bat species. Suitable clustering methods are currently evaluated in collaboration with Naren Ramakrishnan from Virginia Tech's Department of Computer Science. In particular, methods for alternative clustering will be employed as a tool to survey different ways in which the biological shapes can be partitioned. Interactive control over the clustering results by virtue of a "scatter-gather" approach is also in preparation.

The first set of local shape metrics that has been applied to selected shapes (five noseleaves and five outer ears) was based on neighborhoods defined by concentric rings. The rings were obtained by placing spheres around the point (polygon mesh vertex) for which the metric was to be computed and intersecting them with the local shape surface. Along each concentric ring, an number of sample point were placed. Using the central vertex and the sample on the concentric rings, the following shape metrics have been evaluated:

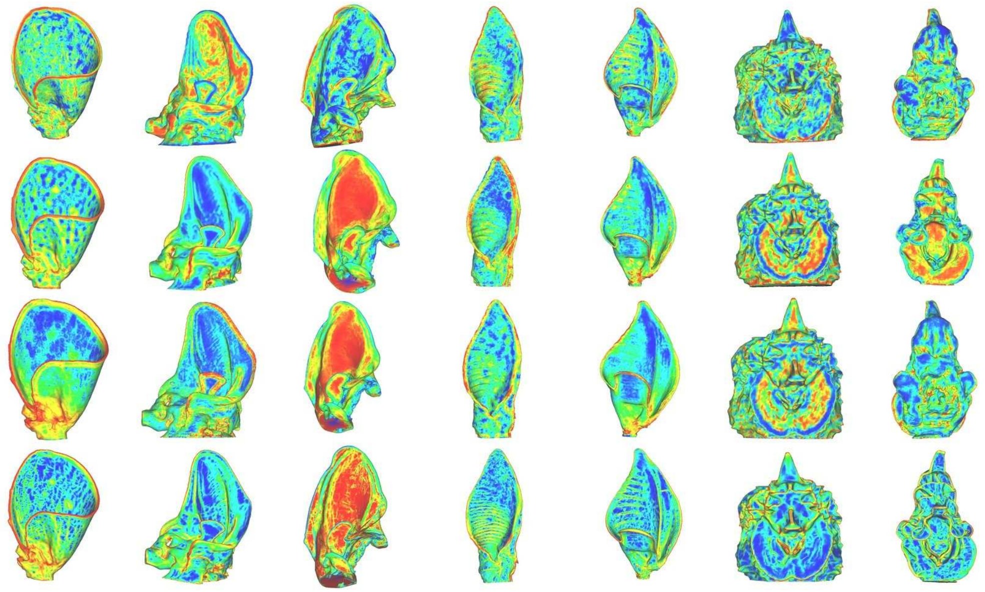

Figure 4: Example of local shape metric applied to example pinna and noseleaf shapes: Principal components of the curvature index (root mean square of principal curvatures) across each shape. Each row shows different raw data being entered in the PCA. Top row: average and standard deviation, second row: 0%, 10%, 50%, 90%, and 100% percentile values, third row: 0%, 10%, 50%, 70%, 90%, and 100% percentile values, bottom row: raw data from each sampling point. The species shown are (columns, from left to right): *Coelops frithii, Taphozous melanopogon, Ia io, Pteropus lylei, Rhinolophus luctus* (ear)*, Rhinolophus affinis, Rhinolophus luctus* (noseleaf).

1. Distance to a plane: a plane was fitted to each concentric ring; the metric is the signed distance of all sample points from the fitted plane.
2. Distribution of surface normals, either computed from the angle that surface normals on the sample point subtend with that of the of the central vertex or among each other
3. Shape diameter function: a measure of the local diameter of the surface
4. Mean curvature: mean value of the principal curvature κ_1, κ_2
5. Gaussian curvature: product of principal curvatures
6. Shape Index: computed from principal curvatures as $\frac{2}{\pi}\arctan\left(\frac{\kappa_1+\kappa_2}{\kappa_1-\kappa_2}\right)$
7. Curvature Index: root mean square of principal curvatures

For each of these seven shape metrics, six different versions were computed resulting in 42 individual descriptors that have been evaluated over all ten shapes in the initial test data set.

The results illustrate the ability of the descriptors to pick up local shape detail with good sensitivity as well as specificity. For example, several of the shape metrics were able to identify the entire rim of the outer

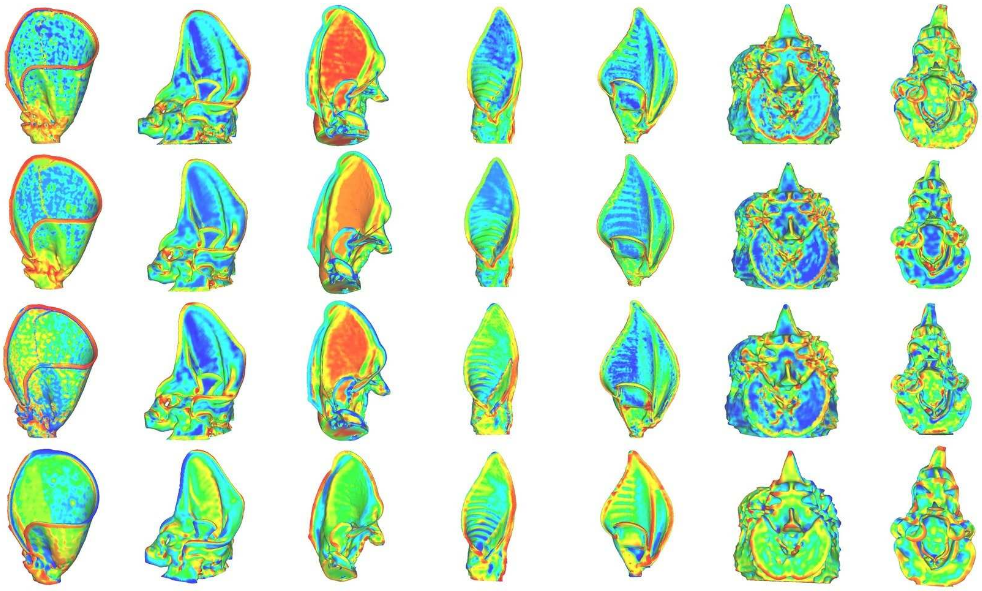

Figure 5: Example of local shape metric applied to example pinna and noseleaf shapes: Principal components of the "distance-to-a-plane" metric (s. text) across each shape. Each row shows different raw data being entered in the PCA. Top row: minimum, maximum, and sum value, second row: average and standard deviation, third row: sum, bottom row: raw data from each sampling point . The species shown are (columns, from left to right): *Coelops frithii, Taphozous melanopogon, Ia io, Pteropus lylei, Rhinolophus luctus* (ear)*, Rhinolophus affinis, Rhinolophus luctus* (noseleaf).

ears in a highly selective manner. These descriptors are currently being used to mark the pinna rim from smoothing. This capability to carry out a selective smoothing of the pinna surfaces without distorting the overall shape of the pinnae will be used to investigate the impact of local shape features on the beampatterns. A smoothing method based on heat kernel smoothing [26] is currently under development for this research.

In order to characterize and classify the unprecedentedly large numbers of beampatterns that have been created by project, characterization methods based on spherical harmonics are currently under development. The spherical harmonics are used to obtain a reduced representation of the beampatterns by virtue of a "power spectrum". For this purpose, the beamgain is mapped onto a set of spherical harmonics that serve as basis functions. The varying degree of the harmonics captures different spatial frequencies over angle in the beampatterns. By summing the coefficients across the different orders of the spherical harmonics of the same degree, the energy contained in the beampattern for the respective spatial frequency is obtained. The results are short vectors (e.g., with six elements for spherical harmonics up to the fifth degree that were used in the first trials) that represent each beampattern. As a pilot experiment to assess the possible utility of these power spectral representations, an attempt was made to classify 20 emission and 20 reception beampatterns using a support vector machine. 80% of the beampatterns were classified correctly as either belonging to emission or reception (s. Figure 7). This initial result supports the hypothesis that the spherical harmonics power spectra are useful and compact representations of the beampatterns. It also raises the interesting possibility that biosonar emission and reception beampatterns are categorically different. This is a though-provoking preliminary finding, because the overall beampattern of an active sonar system is the product of the emission

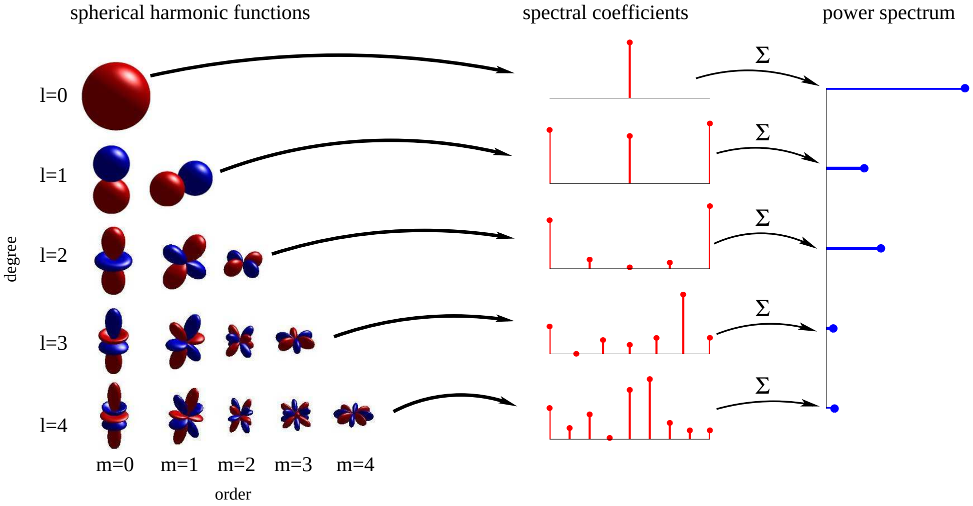

Figure 6: Example of using spherical harmonics to obtain the power spectrum of a beampattern, from left to right: real spherical harmonics used as basis functions for decomposition of the beampattern, weights for each basis function across all degrees and orders, power spectral coefficients obtains by summing the weights across all orders of each degree.

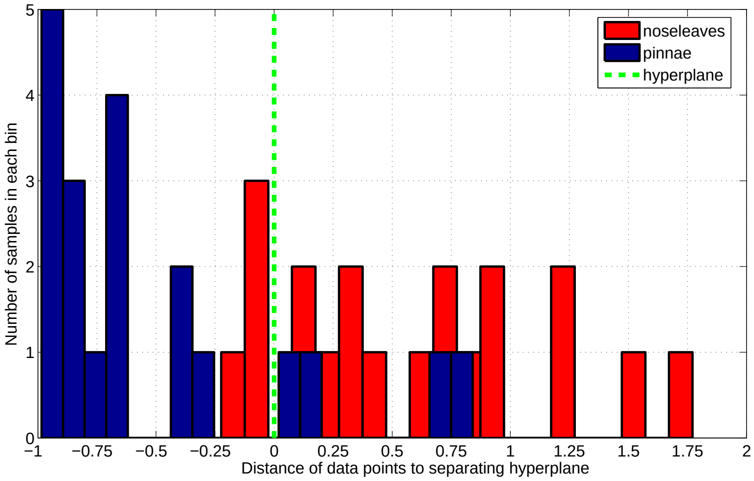

Figure 7: Example of beampattern classification based on spherical power spectra. Beampatterns were classified as either belonging to emission or reception based on the distribution of power in the first five degrees of the spherical harmonics. The separating hyperplane was found using a support vector machine (SVM).

and the reception beampattern. Hence, there should be no separate sets of specifications for he emission and the reception beampatterns. If the categorical difference between emission and the reception beampatterns found in the pilot experiment can be confirmed on a larger data set, it would argue that – at least in biosonar – such separate specifications exist.

In order to align the beampatterns for a quantitative analysis of their natural variability, alignment methods need to be developed as a first step to applying commonly-used methods such as principal component analysis (PCA) for beampatterns alone or canonical correlation analysis (CCA) for linking beampatterns to shapes. At present, experiments with methods based on root-mean-square differences between functions on a spherical domain [5] are under investigation for this purpose. In particular, it still needs to be investigated how the weightings associate with the beampatterns of different frequencies can effect the registration results.

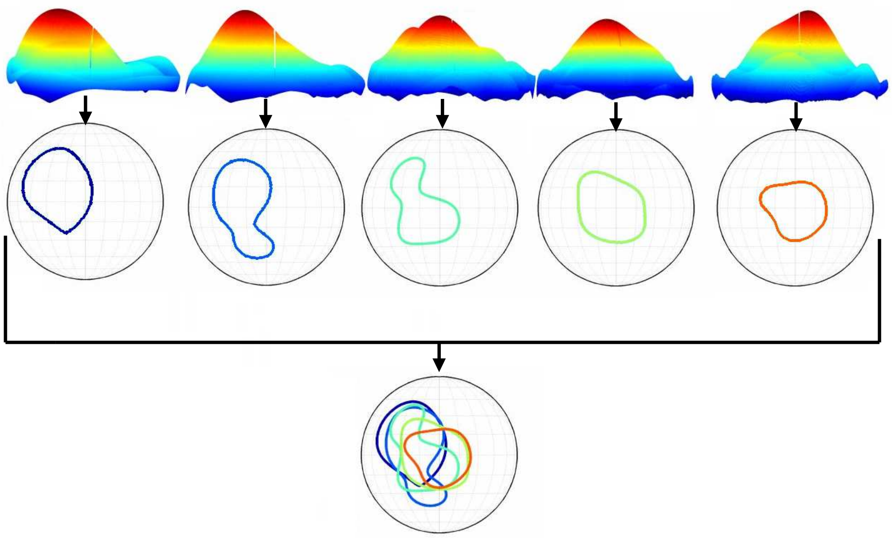

Figure 8: Illustration of the contour maps used to render all noseleaf and outer ear beampattern estimates shown in Figures 9 to 19. Top row: beampattern gains as a function of direction for each frequency (side view), middle row: -3 dB contours for each individual frequency, bottom row: contours for all frequencies superimposed. Frequency is color-coded (blue: low, red: high).

Table 1: List of samples included in data set by taxonomic groups [27].

	scientific name	frequency range	N pinnae	N noseleaves
	Rhinolophidae			
1	*Rhinolophus acuminatus*	60-95 kHz	3	3

2	*Rhinolophus affinis*	70-88.5 kHz	3	3
3	*Rhinolophus sp.(1)*	57.6-87.3 kHz	3	0
4	*Rhinolophus celebensis*	57.6-87.3 kHz	0	3
5	*Rhinolophus sp.(2)*	57.6-87.3 kHz	2	0
6	*Rhinolophus denti*	82-112 kHz	0	3
7	*Rhinolophus ferrumequinum*	72-83 kHz	3	3
8	*Rhinolophus landeri*	105-110 kHz	0	3
9	*Rhinolophus luctus*	32.6-42.6 kHz	3	3
10	*Rhinolophus macrotis*	47.2-53.9 kHz	3	3
11	*Rhinolophus malayanus*	73-90 kHz	2	0
12	*Rhinolophus marshalli*	39.2-42.3 kHz	2	2
13	*Rhinolophus mehelyi*	100-108.6 kHz	0	3
14	*Rhinolophus paradoxolophus*	14-43 kHz	3	3
15	*Rhinolophus pearsoni*	57.6-70 kHz	3	3
16	*Rhinolophus pusillus*	100.3-111.2 kHz	3	3
17	*Rhinolophus rex*	23.7-26.4 kHz	0	2
18	*Rhinolophus rouxi*	35-65 kHz	2	0
19	*Rhinolophus sedulus*	62-76 kHz	0	3
20	*Rhinolophus sinicus*	73.4-87.3 kHz	3	0
21	*Rhinolophus thomasi*	76-86 kHz	4	3
22	*Rhinolophus trifoliatus*	50-53.5 kHz	0	3
23	*Rhinolophus sp.*	57.6-87.3 kHz	3	0
	Pteropodidae			
24	*Rousettus leschenaultii*	8-62 kHz	3	NA
25	*Pteropus lylei*	20-125 kHz[1]	3	NA
26	*Cynopterus brachyotis*	20-125 kHz[1]	2	NA
27	*Cynopterus sphinx*	20-125 kHz[1]	3	NA
28	*Eonycteris spelaea*	20-125 kHz[1]	3	NA
29	*Macroglossus sobrinus*	20-125 kHz[1]	3	NA
	Molossidae			
30	*Tadarida teniotis*	5-15 kHz	3	NA
	Verspertilionidae			
31	*Scotophilus sp.(1)*	36.14-87.15 kHz	3	NA
32	*Scotophilus kuhlii*	36.14-87.15 kHz	4	NA
33	*Scotomanes ornatus*	25-80 kHz	2	NA
34	*Tylonycteris pachypus*	20-100 kHz	2	NA
35	*Plecotus auritus*	21-61 kHz	3	NA
36	*Pipistrellus sp.(1)*	33-100 kHz	1	NA
37	*Pipistrellus sp.(2)*	33-100 kHz	1	NA
38	*Pipistrellus sp.(3)*	33-100 kHz	3	NA
39	*Pipistrellus pipistrellus*	45-78 kHz	1	NA
40	*Pipistrellus nathusii*	35-75 kHz	2	NA
41	*Nyctalus plancyi*	23-88 kHz	2	NA
42	*Nyctalus noctula*	17.3-52.2 kHz	4	NA

---

[1] Species without known active biosonar; the frequency bounds were set from 90% percentiles of all species for which data was available

43	*Barbastella leucomelas*	23-44 kHz	5	NA
44	*Eptesicus serotinus*	23-110 kHz	2	NA
45	*Miniopterus schreibersi*	50-98.5 kHz	4	NA
46	*Murina cyclotis*	37.6-180 kHz	5	NA
47	*Myotis altarium*	40-72 kHz	2	NA
48	*Myotis blythii*	26-107 kHz	6	NA
49	*Myotis formosus*	15-158 kHz	2	NA
50	*Myotis nattereri*	15-137 kHz	2	NA
51	*Myotis ricketti*	26.6-72.5 kHz	3	NA
52	*Kerivoula sp.(1)*	30-189 kHz	6	NA
53	*Myotis sp.(1)*	15-158 kHz	2	NA
54	*Myotis sp.(2)*	15-158 kHz	1	NA
55	*Myotis sp.(3)*	15-158 kHz	1	NA
56	*Myotis sp.(4)*	15-158 kHz	1	NA
57	*Myotis sp.(5)*	15-158 kHz	1	NA
58	*Myotis sp.(6)*	15-158 kHz	1	NA
59	*Ia io*	15-45 kHz	15	NA
	Hipposideridae			
60	*Triaenops persicus*	72-88.5 kHz	0	3
61	*Rhinonicteris aurantia*	109.9-126 kHz	0	3
62	*Aselliscus stoliezkanus*	100-120 kHz	3	3
63	*Asellia tridens*	90-125 kHz	0	3
64	*Coelops frithii*	111-186 kHz	2	3
65	*Hipposideros armiger*	62-125 kHz	3	3
66	*Hipposideros cineraceus*	50-138 kHz	3	3
67	*Hipposideros galeritus*	50-138 kHz	3	3
68	*Hipposideros larvatus*	50-110 kHz	3	3
69	*Hipposideros lylei*	50-138 kHz	2	1
70	*Hipposideros pomona*	98-138 kHz	3	0
71	*Hipposideros diadema*	50-138 kHz	0	3
72	*Hipposideros dyacorum*	50-138 kHz	0	3
73	*Hipposideros cervinus*	50-138 kHz	0	3
74	*Hipposideros commersoni*	50-138 kHz	0	3
75	*Hipposideros caffer*	50-138 kHz	0	3
76	*Hipposideros lankadiva*	60-70 kHz	0	3
	Emballonuridae			
77	*Taphozous melanopogon*	8.29-64.5 kHz	5	NA
	Phyllostomidae			
78	*Vampyrum spectrum*	70-90 kHz	0	3
79	*Vampyriscus bidens*	40-155 kHz	0	3
80	*Trachops cirrhosis*	50-100 kHz	0	3
81	*Sphaeronycteris toxophyllum*	37.8-108 kHz	0	3
82	*Platyrrhinus helleri*	76-131 kHz	0	3
83	*Phyllostomus hastatus*	25-50 kHz	0	3
84	*Phyllostomus discolor*	40-90 kHz	0	3

85	*Lonchophylla thomasi*	20-125 kHz[2]	0	3
86	*Lonchorhina orinocensis*	12-46 kHz[3]	0	1
87	*Erophylla sezekorni*	25-59 kHz	0	3
88	*Diaemus youngi*	41-88 kHz	0	3
89	*Desmodus rotundus*	50-95 kHz	0	3
90	*Chrotopterus auritus*	70-80 kHz	0	3
91	*Centurio senex*	36-106 kHz	0	3
92	*Brachyphylla cavernarum*	17-70 kHz	0	3
93	*Artibeus jamaicenses*	36-106 kHz	0	3
	Nycteridae			
94	*Nycteris aurita*	60-100 kHz	0	3
95	*Nycteris arge*	60-100 kHz	0	3
96	*Nycteris grandis*	60-96 kHz	0	3
97	*Nycteris hispida*	60-100 kHz	0	3
98	*Nycteris intermedia*	60-100 kHz	0	3
99	*Nycteris javanica*	60-100 kHz	0	3
100	*Nycteris macrotis*	60-100 kHz	0	3
101	*Nycteris tragata*	70-100 kHz	0	3
102	*Nycteris thebaica*	61-97 kHz	0	3
	Megadermatidae			
103	*Megaderma lyra*	20-120 kHz	3	3
104	*Megaderma spasma*	40-88 kHz	3	0
105	*Macroderma gigas*	15-70 kHz	0	2
106	*Cardioderma cor*	20-120 kHz	0	3
	total:		185	176

6 Analysis of Shapes

In the current reporting period, work on the analysis of the beamforming shapes in the biosonar system of the bats has focused on using local shape features that have been developed and tested in the previous period. In the current period, clustering methods (scatter, gather, and alternative clustering) have been applied to segment the noseleaf and pinna shapes into components defined by local shape features. This approach has been successful in segmenting out local features such as edges, solitary surface ridges, and washboard patterns [21, 22, 8, 9].

Gather clustering (s. Figure 20) can be used to fuse surface patches that were originally distributed into different classes to segment a noseleaf or ear shape into surfaces and edges [22, 8, 9]. This segmentation is very useful for the removal of local shape features through smoothing since it allows the preservation of the shape's edges and hence the global shape.

Scatter clustering (s. Figure 21) can be used to separate features with high local curvatures on the pinna surface from the pinna edges. In this way, washboard ripple patterns and solitary ridges on the pinna surface can be separated from the pinna edges although the curvature values between the regions overlap [22, 8, 9].

---

[2] No data on biosonar pulses available for species, the frequency bounds were set from 90% percentiles of all species for which data was available

[3] Data on biosonar pulses from related species *Lonchorhina aurita*

Finally, alternative clustering (s. Figure 21) can be used to enhance the resolution for local features, both inside the shape surfaces and also along the rims, where the edge proper can be distinguished from a transition zone [22, 8, 9].

These segmentation techniques have been used to separate the effects of local and global shape features through selective smoothing using a heat kernel filter. This method has been developed during the previous reporting period and have been refined and applied in the course of the current reporting period [2, 3, 17]:

The first results of applying this smoothing method to separate the effect of local and global shape features indicate that local shape features can indeed have a strong impact on the beampattern - but this is not always the case. As may be expected, an important factor for the importance of local features was frequency. For example, it was observed that the free-tailed bat (*Tadarida teniotis*, s. Figure 23) has very pronounced washboard ripple patterns on its pinna, but the effect of removing these pattern through smoothing was limited to the band of the highest frequencies that are known to be used by the animals [23]. This can be explained by the fact that the wavelengths at all but the highest frequencies are much larger than the shape features of the ripple pattern and are hence the ripple does not affect the diffraction process at these frequencies significantly.

For other bat species which use higher frequencies, effects of local shape features were seen throughout the frequency band used by the animals (s. Figures 24, 25).

In the two examples shown here (s. Figures 24, 25), there were also interactions between local surface shape features (washboard ripple) and the tragus - a flap on the pinna rim.

7 Analysis of Diversity in Beampatterns

In the reporting period, the natural variability in the beampatterns has been analyzed using compressed representations of the beampattern functions that have been developed in the previous reporting period. These compressed representations were the power-spectral coefficients derived from a decomposition of the beampattern functions with spherical harmonics [14, 15]. Like a Fourier power spectrum, beam direction and orientations are not conserved in these representations, which is an advantage, since the beampattern estimates have been obtained from isolated ear samples for which the overall pointing direction and orientation are not known.

Multiple comparisons of the power spectral representations have revealed categorical differences in beam shape between evolutionary groupings as well as between emission and reception [14, 15]. The latter observation had been made in the previous reporting period with an overall, black-box classification approach already [14]. In the current period, this remarkable effect was studied in more detail: To exclude a possible confounding effect by different phylogenetic groups, an in-depth analysis was carried out where emission and reception beampatterns were compared within two large taxonomic sister groups (horseshoe bats and old world leaf-nosed bats) that both emit sounds through the nostrils and for which a large number of noseleaf and pinna shape samples were available (s. Table 2). In both groups, beampatterns could be classified as emission or reception with low error probabilities (about 2% for old world leaf-nosed bats, 13% for horseshoe bats). In addition, beampattern differences were found between all the large high-level taxonomic groups (families) represented in the sample. For emission beampatterns, between the sister groups of horseshoe bats and old world leaf-nosed bats on the one hand and the new world leaf-nosed bats on the other (s. Table 2). For reception beampatterns, differences were found when comparing horseshoe bats and old world leaf-nosed bats with vesper bats.

Besides characterizing the separation between functional and phylogenetic beampattern groups, the nature of the differences was also looked into: Looking at the average power spectra for the compared groups

	correct classification [%] ± std.		
	best single feature	best 3 features	FWHM fit
Rhinolophidae & Hipposideridae: noseleaves (98) vs. pinnae (67)	80.0±0.3	86.8±0.4	75.7±1.4
Rhinolophidae: noseleaves (52) vs. pinnae (45)	82.2±0.4	87.0±0.6	75.9±1.9
Hipposideridae: noseleaves (46) vs. pinnae (22)	93.3±0.1	98.1±1.0	86.2±0.6
noseleaves: Rhinolophidae & Hipposideridae (98) vs. Phyllostomidae (46)	72.2±0.8	84.5±2.0	66.8±1.1
pinnae: Rhinolophidae & Hipposideridae (67) vs. Vespertilionidae (72)	89.0±0.2	95.5±1.1	74.6±0.8

Table 2: Examples of correct rates of beampattern classification based on spherical power spectra. Beampatterns are classified as either belonging to one of the two populations in each group. The separating hyperplane is found using a Support Vector Machine. Rates acquired with subsets of one and three features, that minimize the classification error, chosen from the 150 variables by feature selection method are shown. The last column presents the best classification rate for heat kernel fits using Full Width at Half Maximum (FWHM). For numerical beampattern estimates and for heat kernel fits, a bootstrap has also been run on the classifications and the error measures on the results (variation from average) are presented [15].

(s. Figure 26), differences in the spectral level for the medium and higher degrees of the spherical harmonics are the most obvious [14, 15]. Since higher degrees of the spherical harmonics represent higher spatial frequencies and due to the reciprocity between the spatial and the frequency domain, this can be taken as an indication for the existence of differences in beamwidth between the groups [14, 15]. This hypothesis was tested by replacing the actual beampatterns with fits of heat kernel functions [1, 7]. The width of the resulting heat kernel fits was than used as a classification feature and was able to deliver a classification performance (67 to 86%, s. Table 2) that was significantly reduced from the results obtained with the original data, but still demonstrated a separation in beamwidth between all investigated groups. The reduction in performance can be seen as indication that the beampatterns differ not only in beamwidth but also in other parameters.

The finding that different phylogenetic bat groups differ in their average beampatterns (in particular beamwidth, but also other aspects) could be interpreted as possible adaptations to the different sonar sensing tasks and environmental constraints that these groups are facing. The functional significance of the categorical differences between emission and reception beams remains unclear and is hard to reconcile with a linear signal processing theory of sonar function where these two beampatterns would just be multiplied with each other. All the more, it is remarkable that such a strong separation could be established in fairly large data sets from two (sister) bat families.

Besides the differences in the means between each of the studied groups, the variability in the beampattern within each group was also studied. For this purpose, a principal component analysis (PCA) of the beampatterns in each group was carried out (s. Figure 28). The results show similarities as well as differences [14, 15]. For the noseleaves, the eigenvectors associated with the three largest eigenvectors, show an overall similar mapping into the space of the original spherical harmonics power spectra for horseshoe bats, old world leaf-nosed bats, and new world leaf-nosed bats. Since the former two families are sister groups, this finding is not as remarkable as the similarity between these two families and the new world leaf-nosed bats which are phylogenetically very distant [10]. In contrast to the situation for the emission beampatterns, the comparisons of the variability in the different pinna beampatterns show that the variability even in the sister families of horseshoe bats and old world leaf-nosed bats differ noticeably, although again some general similarities between the distribution patterns exist [14, 15]. These similarities could indicate that in all these studied groups, the natural variability has been shaped by the same general design rules. At the same time, the apparent differences could indicate that the biosonar system has been tuned to different sensing tasks and constraints in each group.

7.1 Dynamic Shape Features

Local shape features of the noseleaves and pinnae of bats do not only change from species to species, but in some species can be changed through muscular actuation in each individual animal [20]. These dynamic, controlled changes to the shapes are of potential importance for biosonar function [13, 18] and hence we wanted to put them into the context of the interspecific diversity. In order accomplish this, we have developed ways in which computer animation techniques can be applied to digital shape models of bat noseleaves and pinna to recreate these behavioral variations in an interactive fashion and study their impact on the acoustic characteristics of the device (s. Figure 29).

Our numerical beampattern predictions of the deformed shapes indicate that such shape-reconfiguration behaviors can have an impact on the acoustic characteristics of the baffle shapes (s. Figure 30). Furthermore, we have found one dynamic feature, the rotation of the so-called “lancet” in the of noseleaf of the greater horseshoe bat (*Rhinolophus ferrumequinum*), that had a very robust and consistent impact on the beampattern: Rotating the lancet forward caused a redistribution of emitted energy from a single mainlobe in the beampattern into multiple sidelobes (s. Figure 31).

8 Analysis of Diversity in Beampatterns

In order to be able to carry out an analysis of variability in the beampatterns, the sets of multiple beampatterns (one for each frequency) obtained for each shape sample (noseleaf or outer ear) first need to be aligned. Over the last reporting period, we have worked on this alignment problem and have found a promising solution. We have settled on quantifying the alignment between two beampatterns by a p-norm [4]. The exponent p of the p-norm allows us to influence the weighting of large and small features of the beampatterns (e.g., the mainlobe and the sidelobe) [4].

The goal of the alignment procedure is then to minimize the value of the p-norm between two sets of beampatterns. The optimization space is given by all possible rotations. We have found that the overall location of the mainlobes of the beampatterns in the alignment determines the overall layout of the cost function: Since the mainlobes are to a first approximation rotation symmetric, there is an entire manifold of rotations that can align the mainlobes from two beampatterns. Along this manifold, the value of the cost function will vary due to local features, in particular asymmetries, of the beampatterns (s. Figure 32). Hence, the search for the best alignment (minimum in the cost function) can be constrained to the vicinity of this manifold of rotations. This provides an advantage in computational efficiency over searches through the entire rotation space [19] that is significant when aligning our entire data set of 361 beampattern sets. In all beampattern combinations tested so far, the natural asymmetries in the beampatterns – combined with a suitable value of p – have resulted in a unique global minimum. Hence, from our testing up to now, it appears that our beampattern alignments are least unique and stable (s. examples in Figure 32). We are about to deploy it around a larger set of beampatterns and then use the results to carry out a PCA to characterize the natural variability in terms of “eigenbeams”. This work will extend our previous results on the differences between beampattern classes [16] to give us a better understanding how the natural variability in these beampattern classes differs.

9 Summary of the Most Important Results

- The research has created an unprecedented data set that contains digital shape models of emitting and receiving baffles of bats along with numerical estimates of the corresponding beampatterns.
- For the ear shapes, the following was accomplished:
  - decomposition of the shapes into local shape features
  - analysis of the acoustic contributions of shape features to acoustic device properties (beampatterns)
  - reproduction of local shape features in biomimetic pinna model
  - interactions of static and dynamic features
- for the acoustic characteristics (beampatterns), the following was accomplished:
  - compression of beampattern data using spherical harmonics; used to demonstrate taxonomic and functional differences in the beampatterns
  - developed methods for beam alignment and eigenvector-based ("eigenbeam") decomposition of beampatterns; the results show that the overall shape of the beampatterns can be explained with a small number of eigenbeams that capture beamwith change with frequency in a "center-surround" mechanism.

10 Conclusions

By analyzing a large high-resolution beampattern data set, it has been established that bat biosonar beampatterns are fundamentally different from the directional characteristics of most engineered devices with a similar function. Whereas the engineered devices, e.g., sonar and radar emitters and receivers are optimized to provide simple beampatterns with a narrow mainlobe and weak sidelobes, bat biosonar beampatterns have much more complicated shapes with multiple strong lobes separated by deep notches. Due to the small size of the animals compared to the wavelengths they use, the beampatterns are – by necessity – much wider than what is usually deemed necessary in engineered systems. The greater shape complexity of the noseleaves, pinnae, and the beampatterns they produce suggests that bats use a very different approach to providing sensory information that can meet the needs of autonomous navigation in structure-rich natural environments. Since the approach taken by the bats is much more powerful and parsimonious than what has been accomplished in engineering, bats are highly recommended as a model system for the design of sensing in autonomous outdoor platforms. The analysis of the biodiversity presented here also indicates that bats have found ways to customize their biosonar systems for different sensory tasks and circumstances under which they have to be performed which could be a source for information on how to better customized engineered sensing.

References

[1] N. Berline, E. Getzler, and M. Vergne. *Heat kernels and Dirac operators*. Springer Verlag, 1992.

[2] L. Cai, M. Motamedi, and R. Müller. Engineering analysis of biosonar beampatterns across different bat species. Presented at: First Interdisciplinary Research Symposium, Blacksburg VA, November 2011.

[3] L. Cai, Q. Xu, W. Mio, C. Grimm, and R. Müller. Functional effects of local shape features in the bat biosonar system. Presented at: NSF IBIV Meeting at Histochemistry 2012, Woods Hole, MA, March 2012.

[4] P. Caspers, R. Pan, A. Leonessa, and R. Müller. The alignment problem for bat biosonar beampatterns. *Proc. Meet. Acoust.*, 19:010007, 2013.

[5] E.A. Coutsias, C. Seok, and K.A. Dill. Using quaternions to calculate rmsd. *J. Comp. Chem.*, 25(15):1849–1857, 2004.

[6] M. Garland and P.S. Heckbert. Surface simplification using quadric error metrics. In *Proceedings of the 24th Annual Conference on Computer Graphics and Interactive Techniques*, pages 209–216. ACM Press/Addison-Wesley Publishing Co., 1997.

[7] A. Grigoryan. *Heat kernel and Analysis on manifolds*, volume 47. Amer Mathematical Society, 2009.

[8] M. S. Hossain, O.P.K. Reddy, C. Grimm, R. Müller, L. T. Watson, and N. Ramakrishnan. Scatter/gather clustering: Flexibly incorporating user feedback to steer clustering results. In *Proceedings of the IEEE Conference on Visual Analytics Science and Technology*. in press.

[9] M. S. Hossain, O.P.K. Reddy, C. Grimm, R. Müller, L. T. Watson, and N. Ramakrishnan. Scatter/gather clustering: Flexibly incorporating user feedback to steer clustering results. *IEEE Transactions on Visualization and Computer Graphics*, 2012. in press.

[10] G. Jones and E. C. Teeling. The evolution of echolocation in bats. *Trends Ecol. Evol.*, 21(3):149–56, Mar 2006.

[11] T. Ju. Robust repair of polygonal models. In *ACM Transactions on Graphics*, volume 23, pages 888–895. ACM, 2004.

[12] William E. Lorensen and Harvey E. Cline. Marching cubes: A high resolution 3d surface construction algorithm. In *Computer Graphics (Proceedings of SIGGRAPH '87)*, volume 21, pages 163–169, 1987.

[13] S. Z. Meymand, M. Pannala, and R. Müller. Characterization of the time-variant behavior of a biomimetic beamforming baffle. *J. Acoust. Soc. Am.*, 133(2):1141–1150, February 2013.

[14] M. Motamedi, Lvyin Cai, and R. Müller. Characterization of shape diversity in bat biosonar beampatterns. *J. Acoust. Soc. Am.*, 130(4):2562, October 2011.

[15] M. Motamedi and R. Müller. Characterization of the biodiversity in bat biosonar beampatterns with spherical harmonics. *J. Acoust. Soc. Am.*, 2012. in prep.

[16] M. Motamedi and R. Müller. Characterization of the biodiversity in bat biosonar beampatterns with spherical harmonics. *J. Acoust. Soc. Am.*, 135(6):3613–3619, June 2014.

[17] R. Müller, L. Cai, M. Motamedi, O. P. K. Reddy, C. Grimm, and W. Mio. The role of shape in the biosonar system of bats. Presented at: NSF IBIV Meeting at Histochemistry 2012, Woods Hole, MA, March 2012.

[18] R. Müller, L. Feng, and M. Pannala. Bat biosonar as an inspiration for dynamic sensing. In *Proceedings of the SPIE*, volume 8686, pages 86860I–1–7 (7pages), April 2013.

[19] R. Pan, V. Skala, and R. Müller. Globally optimal rotation alignment of spherical surfaces with associated scalar values. *3D Res.*, 4(3):3, September 2013.

[20] M. Pannala, S.Z. Meymand, and R. Müller. Interplay of static and dynamic features in biomimetic smart ears. *Bioinsp. Biomim.*, 8(2):026008 (9 pages), May 2013.

[21] O.P.K. Reddy, C. Grimm, M. Hossain, and R. Müller. Engineering analysis of beamforming shapes in bat biosonar. Presented at: First Interdisciplinary Research Symposium, Blacksburg VA, November 2011.

[22] O.P.K. Reddy, M.S. Hossain, N. Ramakrishnan, C. Grimm, and R. Müller. Clustering of local shape features in the bat biosonar system. Presented at: NSF IBIV PI Meeting, Woods Hole, MA, March 2012.

[23] D. Russo and G. Jones. Identification of twenty-two bat species (mammalia: Chiroptera) from italy by analysis of time-expanded recordings of echolocation calls. *Journal of Zoology*, 258(1):91–103, 2002.

[24] W. Schroeder, K. Martin, and B. Lorensen. *The Visualization Toolkit An Object-Oriented Approach To 3D Graphics*. Kitware, Inc., 4th edition, 2006.

[25] W.J. Schroeder, J.A. Zarge, and W.E Lorensen. Decimation of triangle meshes. In *Computer Graphics*, volume 26, pages 65–70, 1992.

[26] S. Seo, M. Chung, and H. Vorperian. Heat kernel smoothing using laplace-beltrami eigenfunctions. *Medical Image Computing and Computer-Assisted Intervention–MICCAI 2010*, pages 505–512, 2010.

[27] N.B. Simmons. *Mammal species of the World: a taxonomic and geographic reference*, volume 1, chapter Order Chiroptera, pages 312–529. Johns Hopkins University Press, 3rd edition, 2005.

[28] Q.Y. Zhou, T. Ju, and S.M. Hu. Topology repair of solid models using skeletons. *IEEE Transactions on Visualization and Computer Graphics*, pages 675–685, 2007.

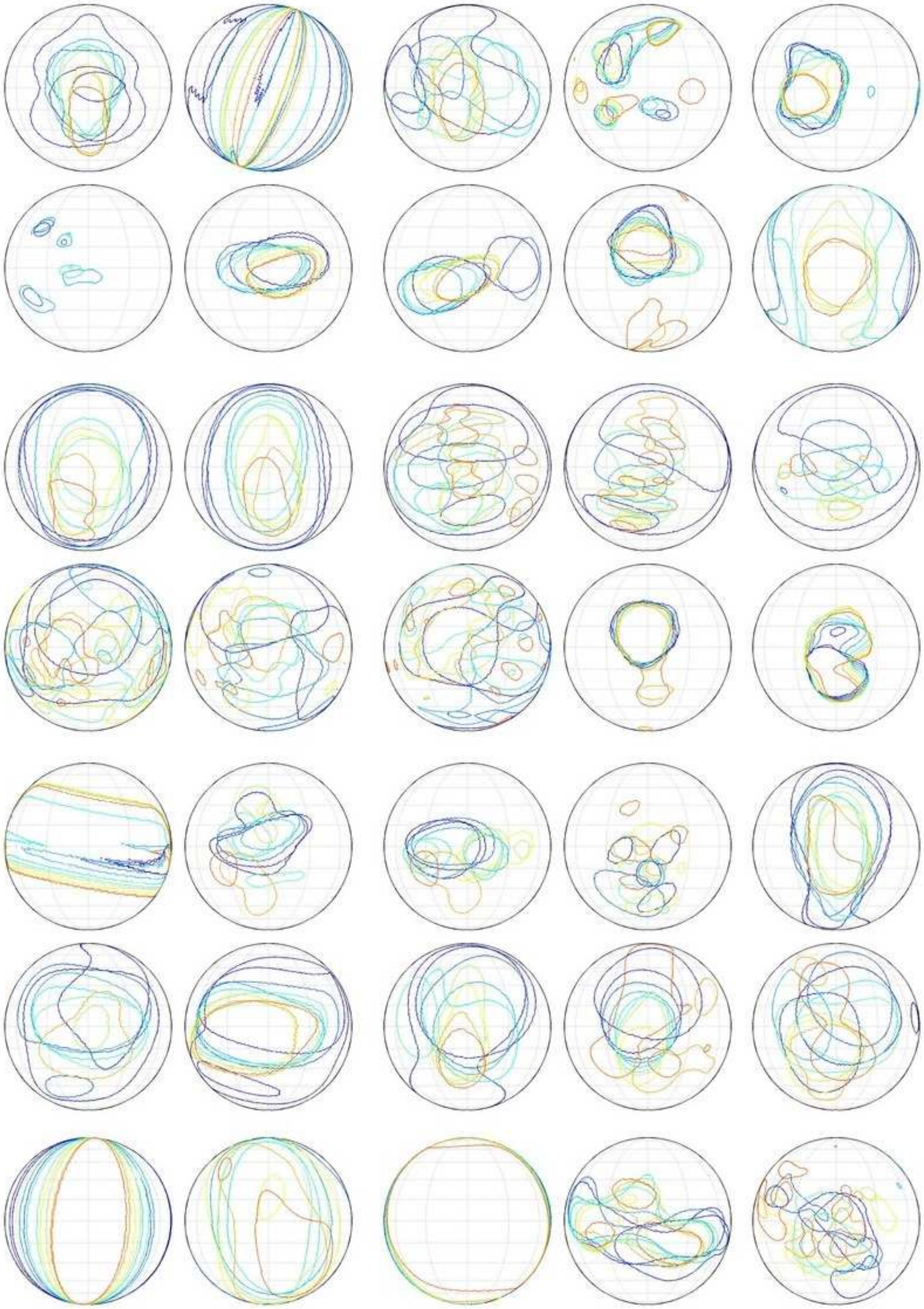

Figure 9: Contour map renderings (s. Figure 8) of numerical beampattern estimates obtained for the different noseleaf shapes in the data set.

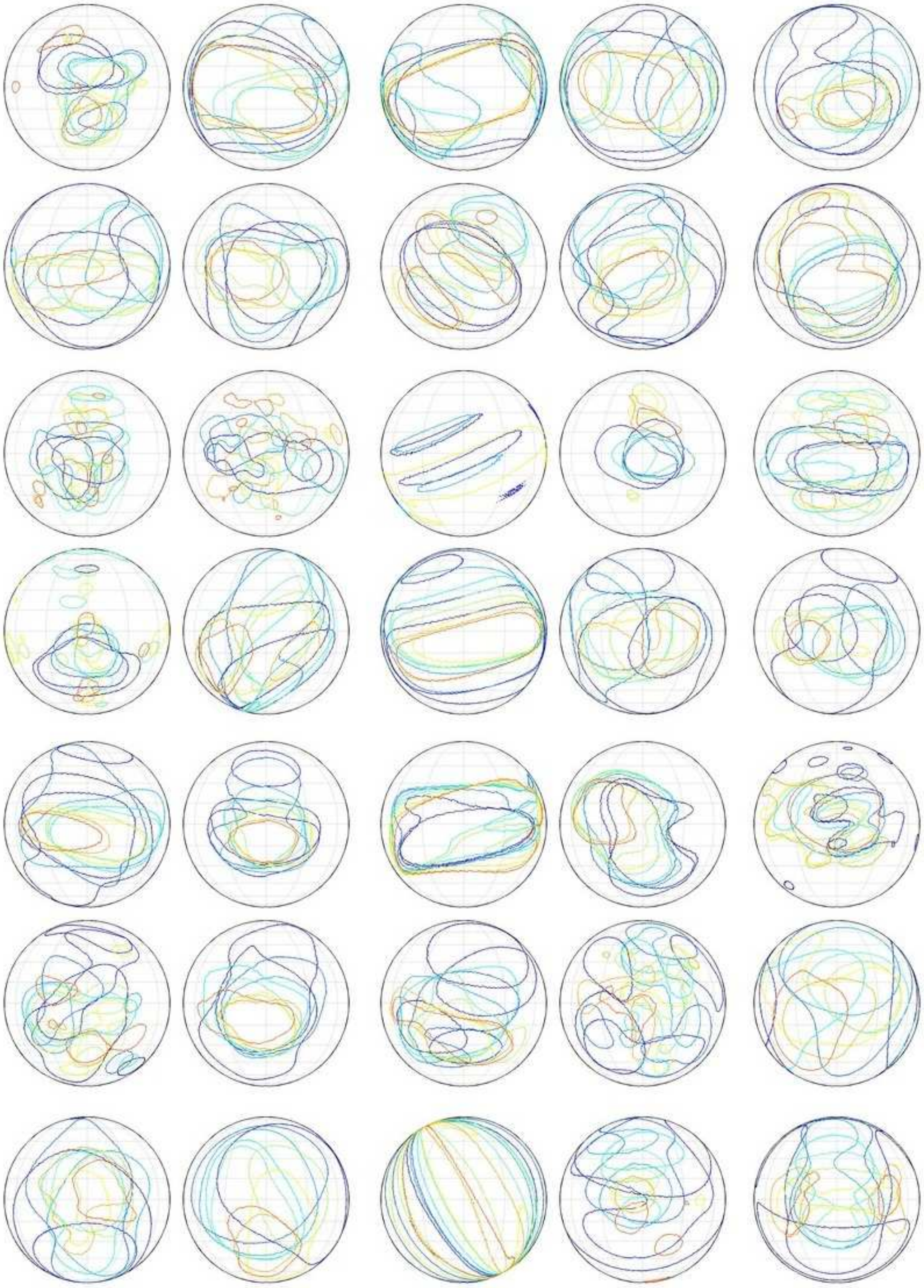

Figure 10: Contour map renderings (s. Figure 8) of numerical beampattern estimates obtained for the different noseleaf shapes in the data set (continued).

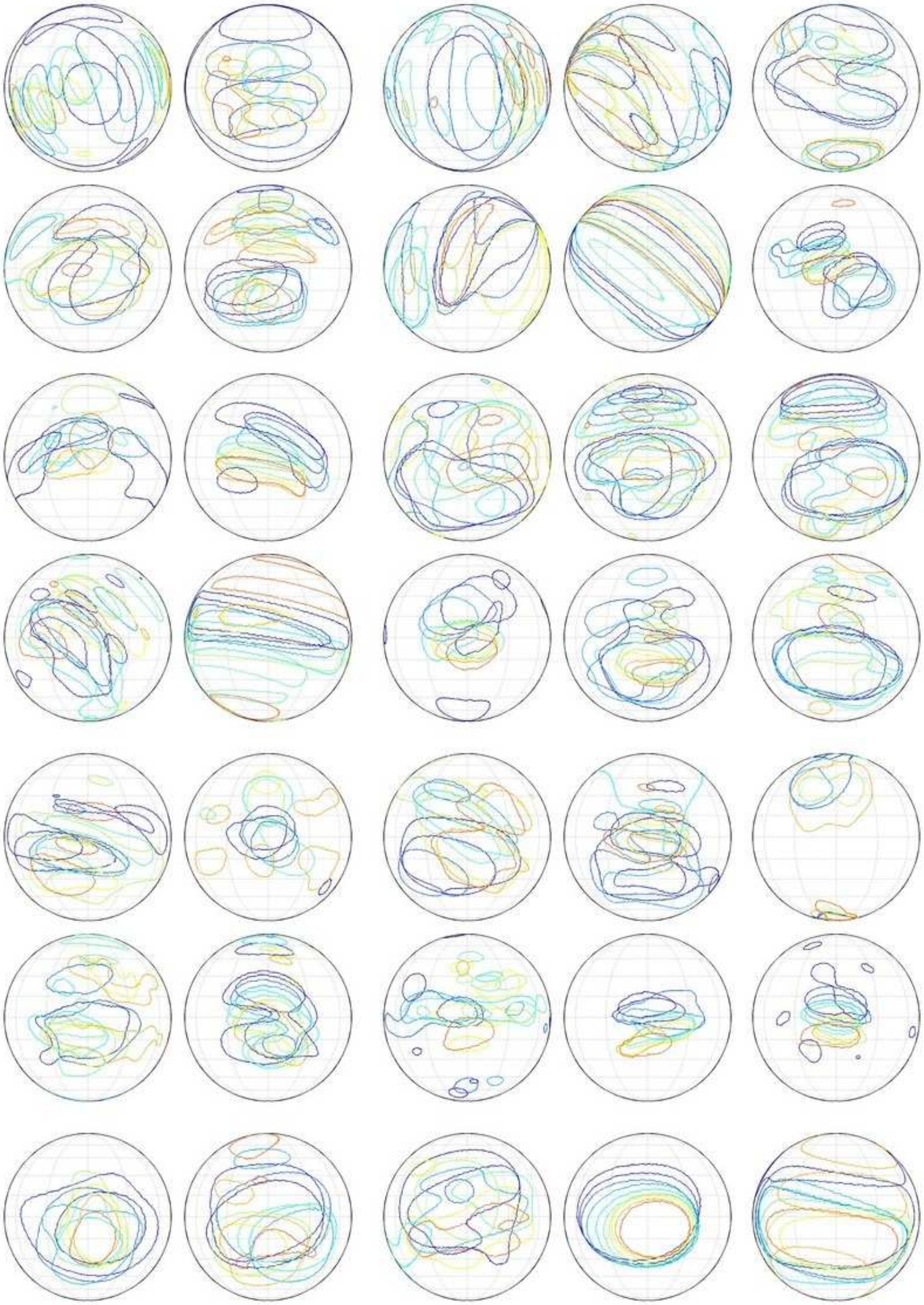

Figure 11: Contour map renderings (s. Figure 8) of numerical beampattern estimates obtained for the different noseleaf shapes in the data set (continued).

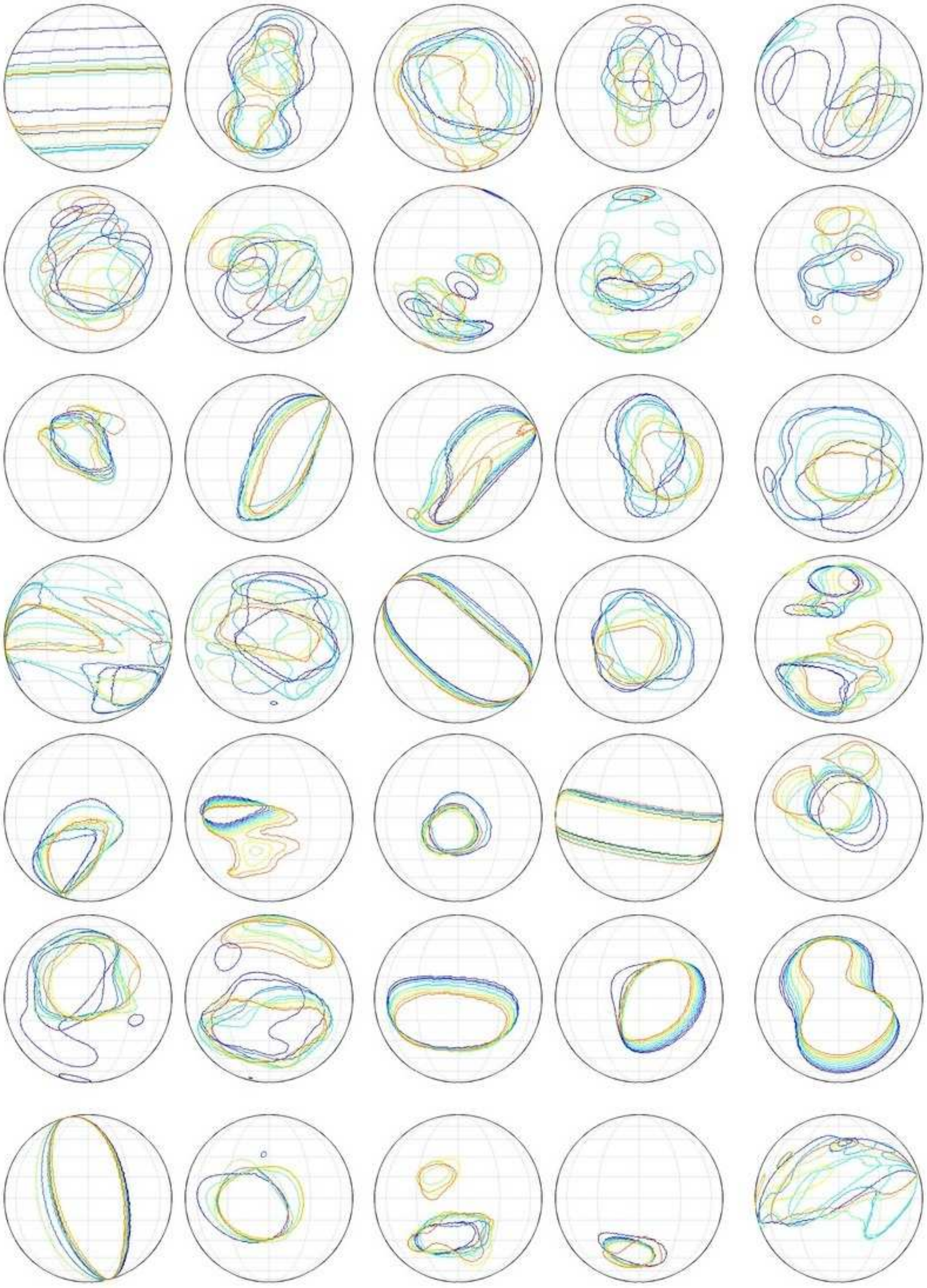

Figure 12: Contour map renderings (s. Figure 8) of numerical beampattern estimates obtained for the different noseleaf shapes in the data set (continued).

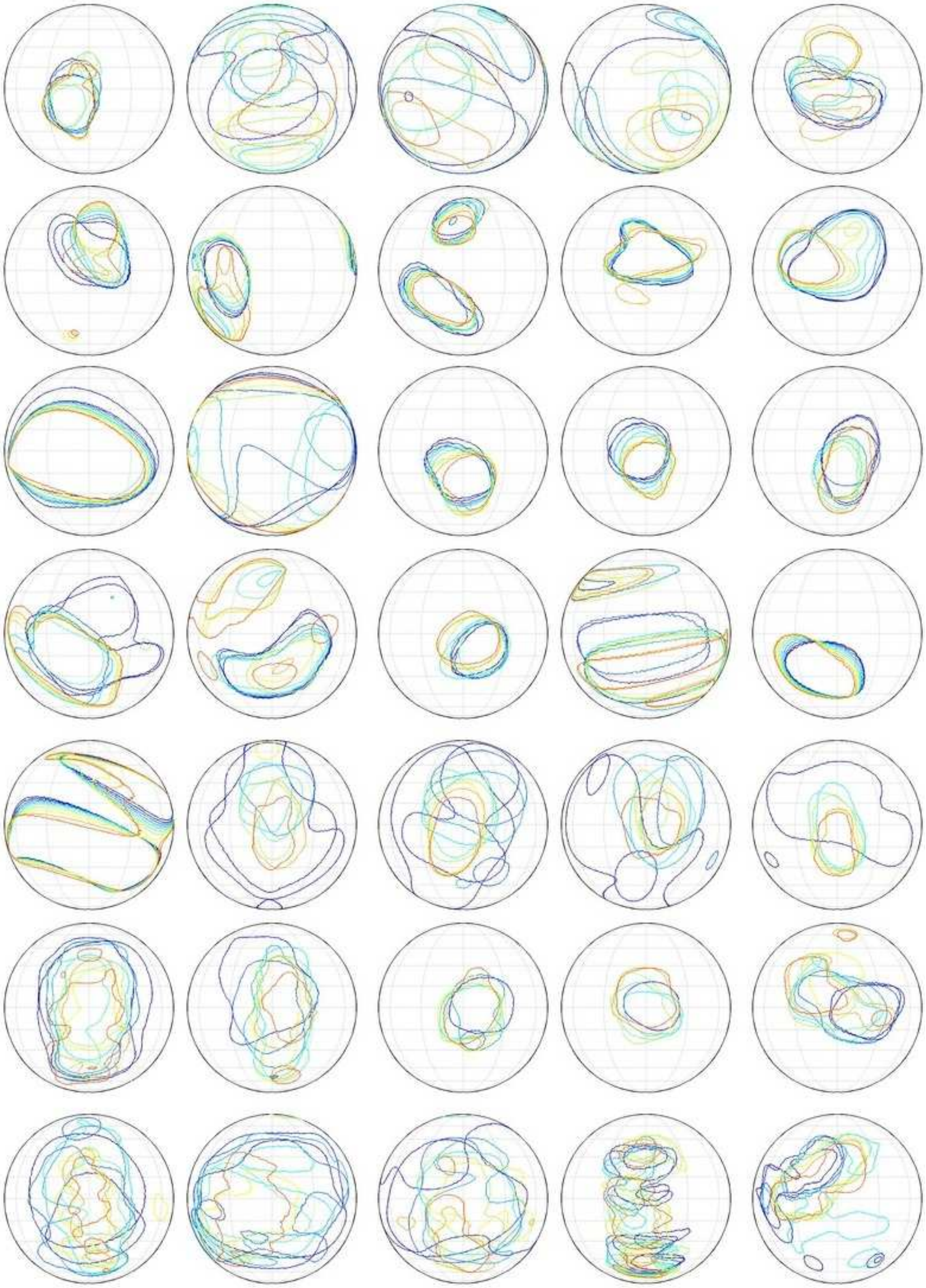

Figure 13: Contour map renderings (s. Figure 8) of numerical beampattern estimates obtained for the different noseleaf shapes in the data set (continued).

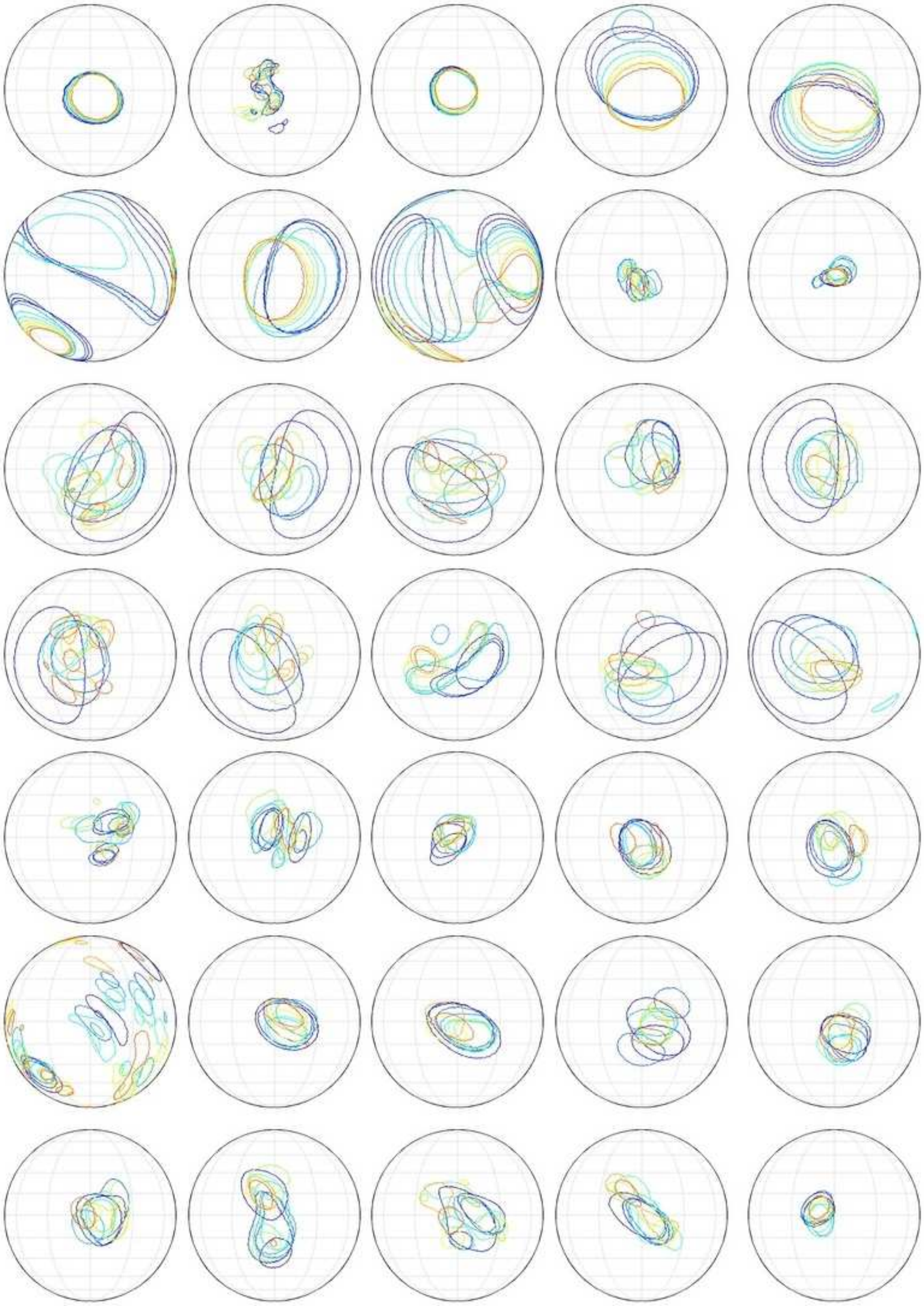

Figure 14: Contour map renderings (s. Figure 8) of numerical beampattern estimates obtained for the different outer ear shapes in the data set.

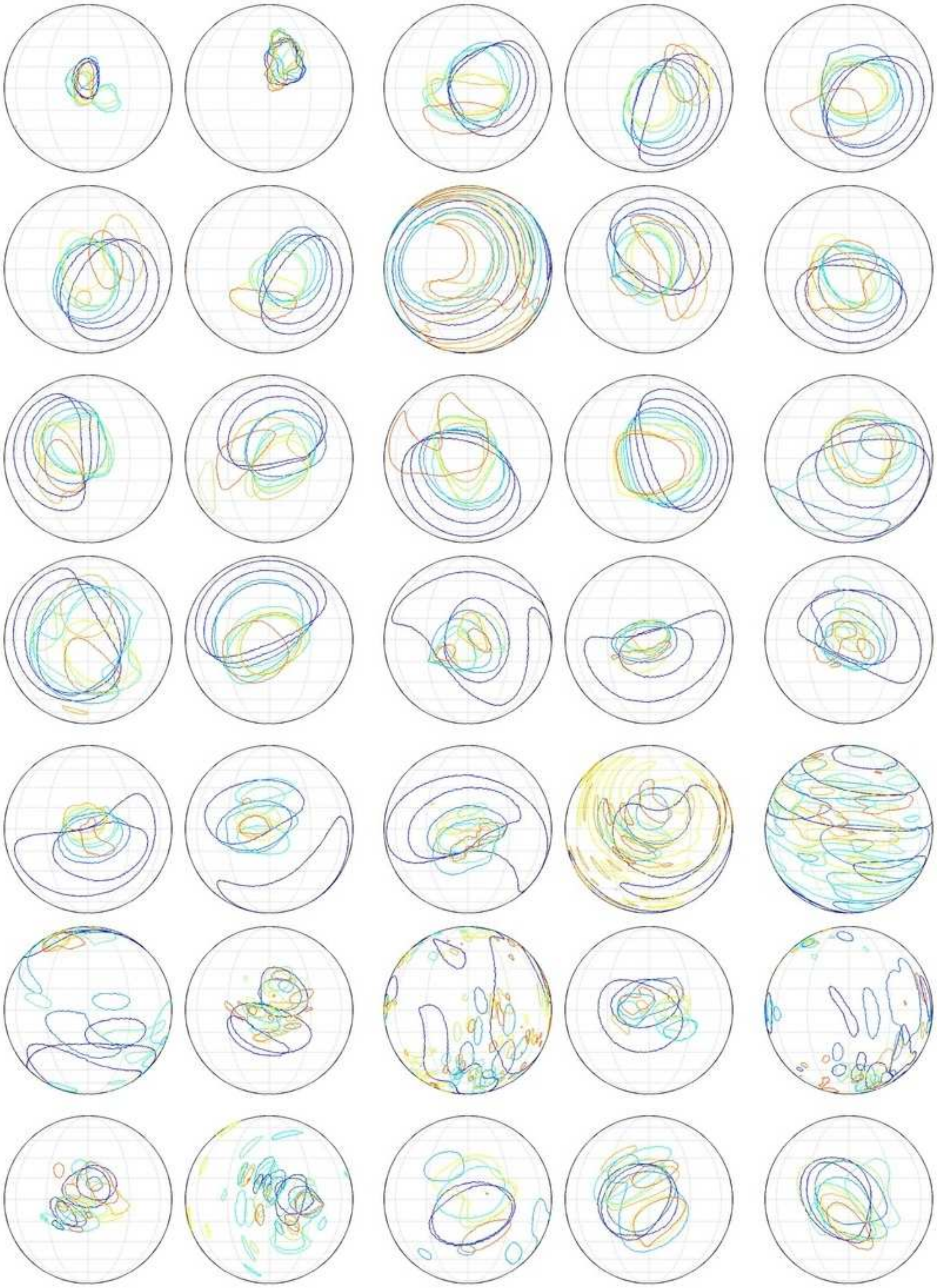

Figure 15: Contour map renderings (s. Figure 8) of numerical beampattern estimates obtained for the different outer ear shapes in the data set (continued).

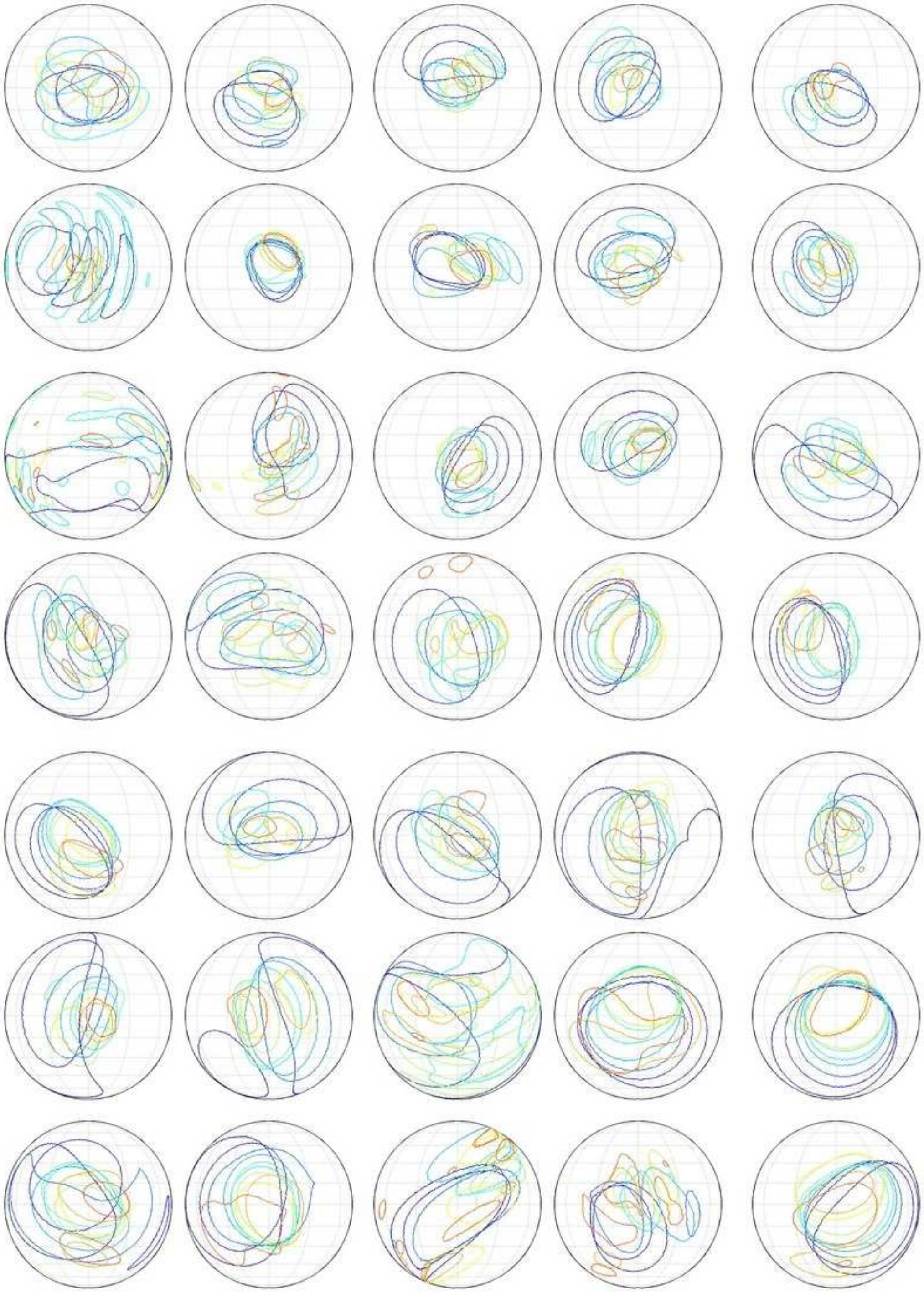

Figure 16: Contour map renderings (s. Figure 8) of numerical beampattern estimates obtained for the different outer ear shapes in the data set (continued).

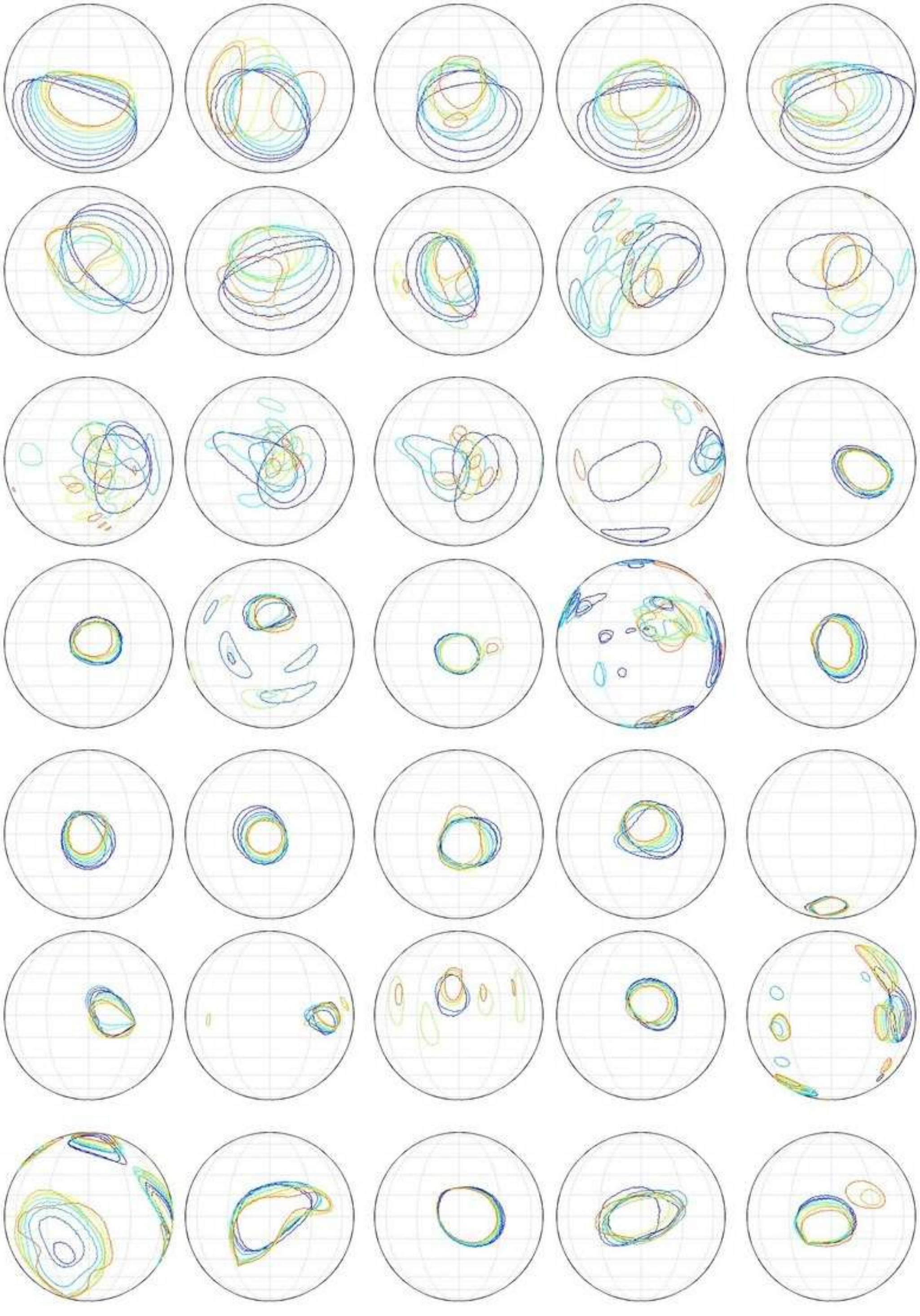

Figure 17: Contour map renderings (s. Figure 8) of numerical beampattern estimates obtained for the different outer ear shapes in the data set (continued).

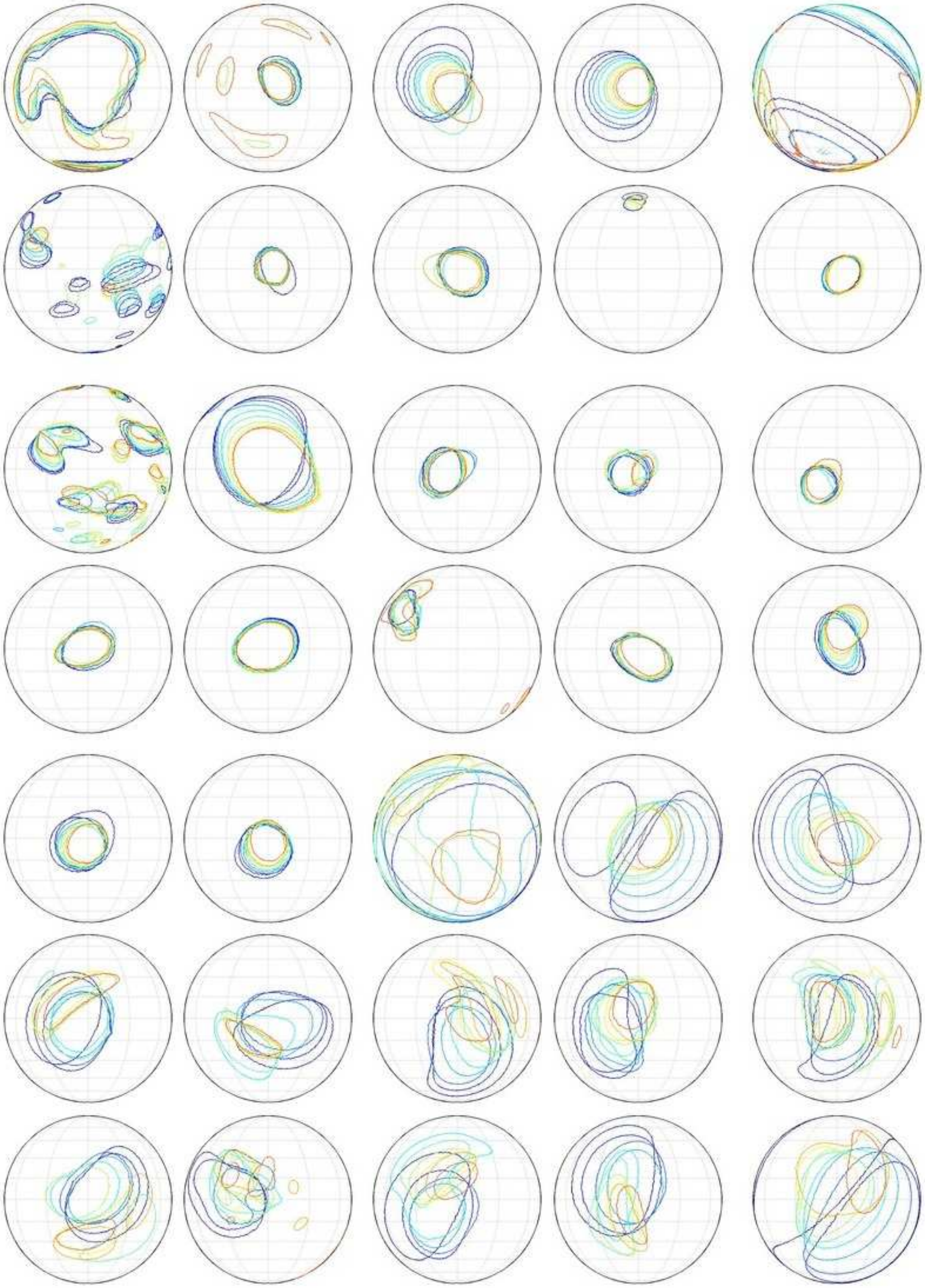

Figure 18: Contour map renderings (s. Figure 8) of numerical beampattern estimates obtained for the different outer ear shapes in the data set (continued).

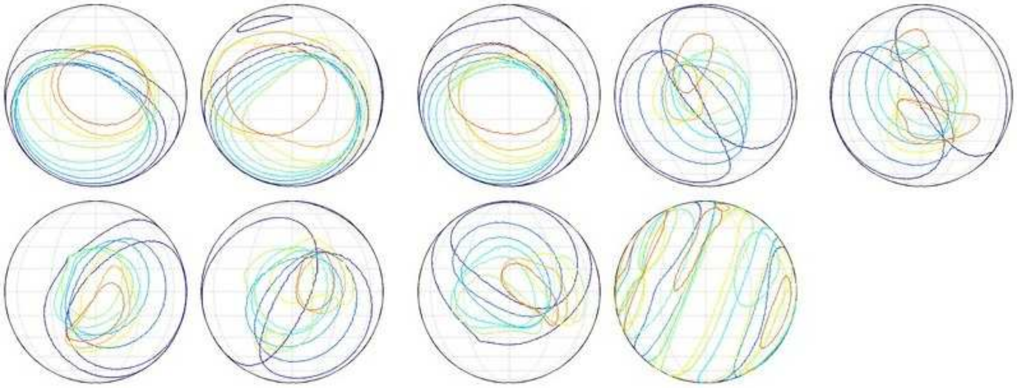

Figure 19: Contour map renderings (s. Figure 8) of numerical beampattern estimates obtained for the different outer ear shapes in the data set (continued).

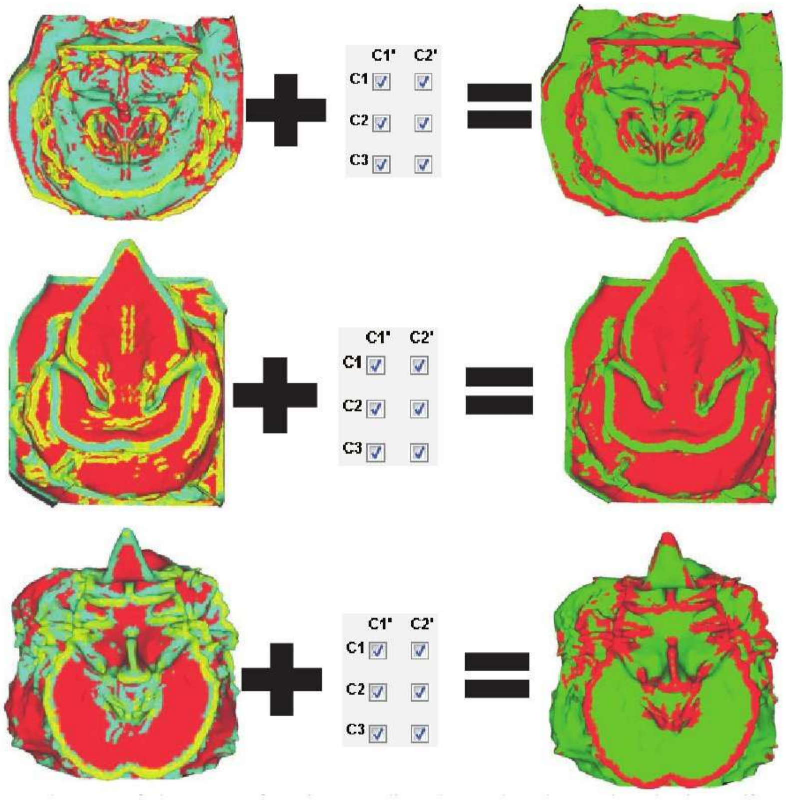

Figure 20: Examples of gather clustering: Combining three clusters into two yields segmentations of different noseleaf shapes that are able of separating edges from surfaces. From top to bottom: giant leaf-nosed bat (*Hipposideros commersoni*), greater spear-nosed bat (*Phyllostomus hastatus*), intermediate horseshoe bat (*Rhinolophus affinis*).

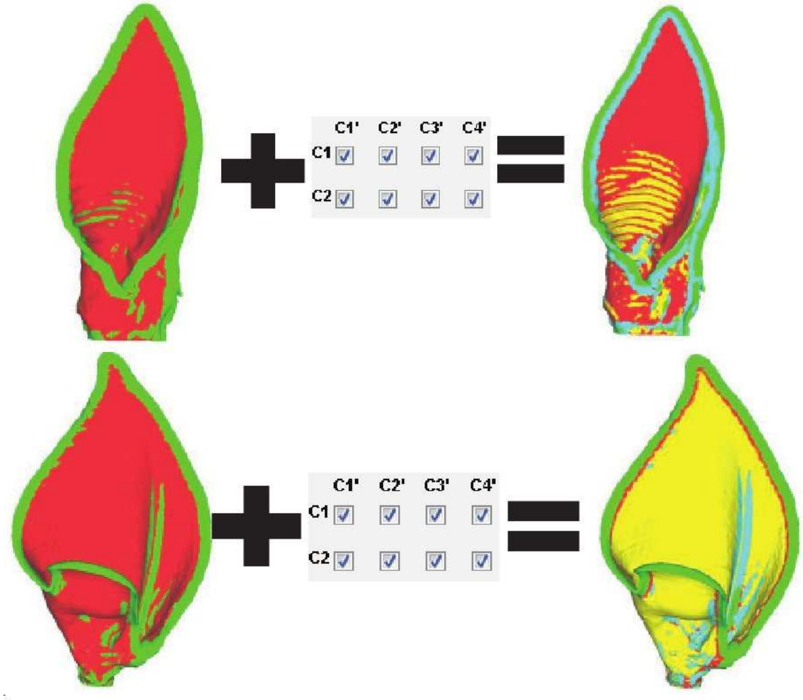

Figure 21: Examples of scatter clustering: By redistributing the surface areas of two clusters into three, local shape features such as washboard ripple patterns (top row) and single ridges (bottom row) can be segmented out as distinct entities. Top row: Lyle's flying fox (*Pteropus lylei*), bottom row: Woolly horseshoe bat (*Rhinolophus luctus*).

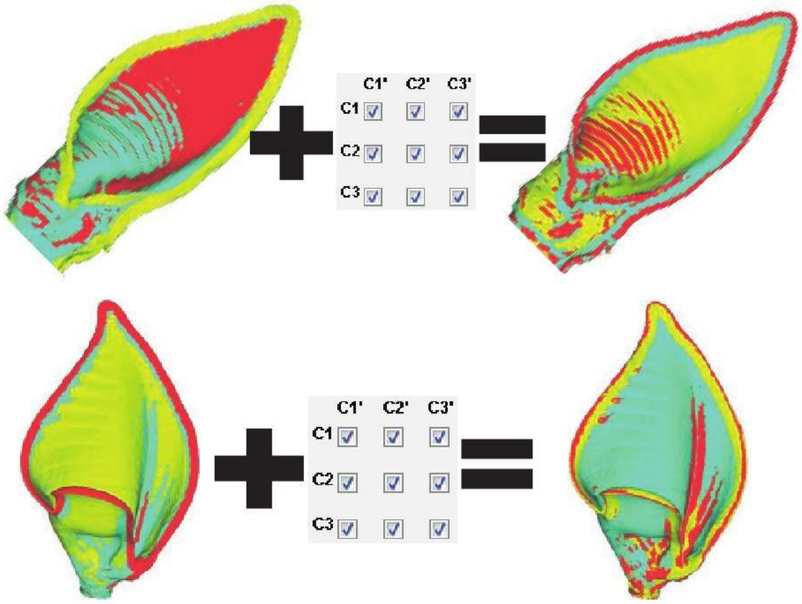

Figure 22: Examples of alternative clustering: Alternative clusterings can result in a better resolution for local features such as ripple patterns (top) or isolated ridges (bottom). Top row: Lyle's flying fox (*Pteropus lylei*), bottom row: Woolly horseshoe bat (*Rhinolophus luctus*)

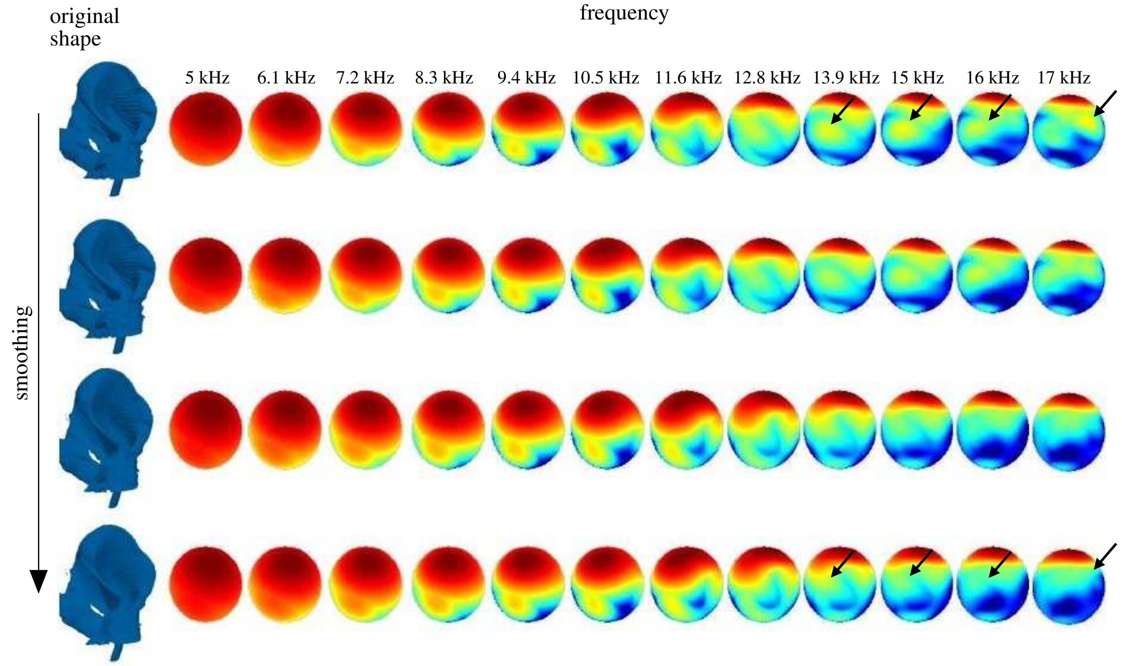

Figure 23: Example of local shape features that appear to have little impact at low frequencies, but have an effect on sidelobe formation (arrows) at high frequencies (*Tadarida teniotis*).

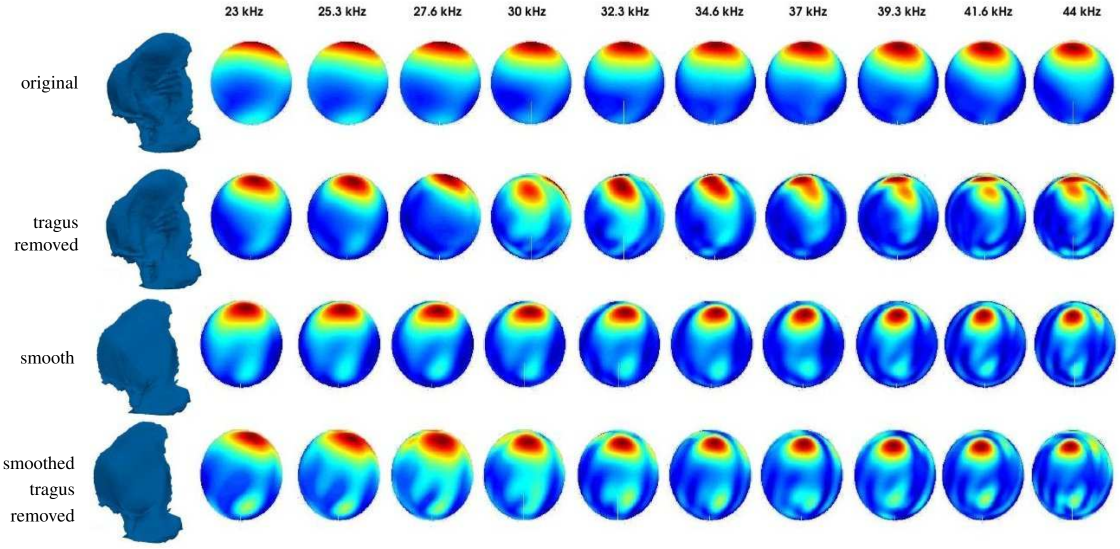

Figure 24: Example of local shape features that appear to have little effect presumably because they much smaller than the relevant wavelengths (genus Barbastella).

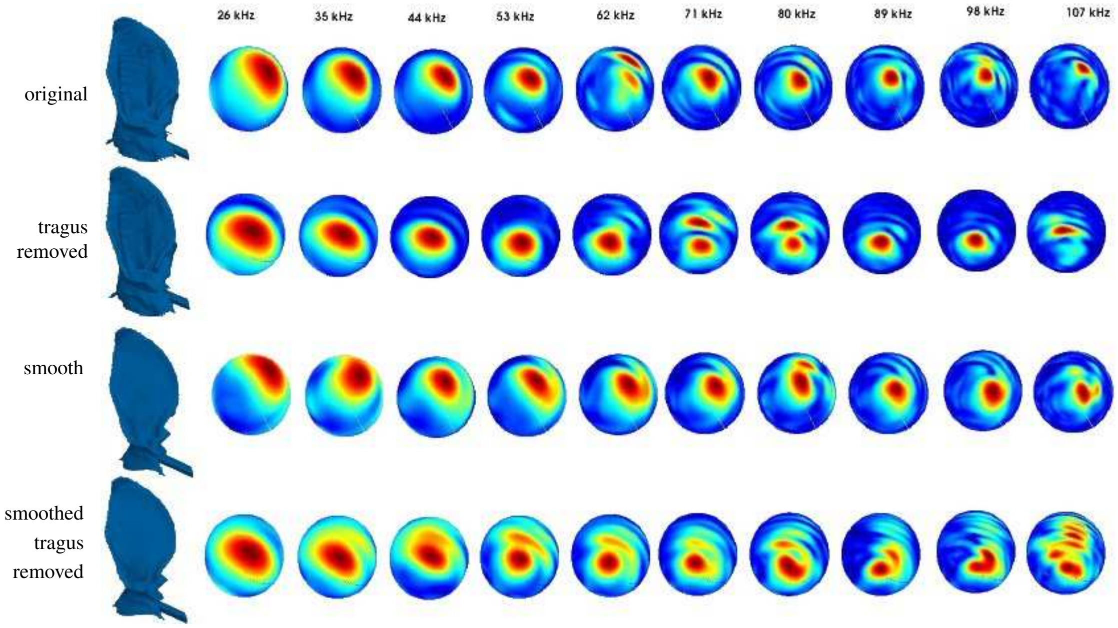

Figure 25: Example of local shape features that have an effect on the beampattern and also show interactions, in this case between a washboard ripple pattern and a prominent tragus (Myotis).

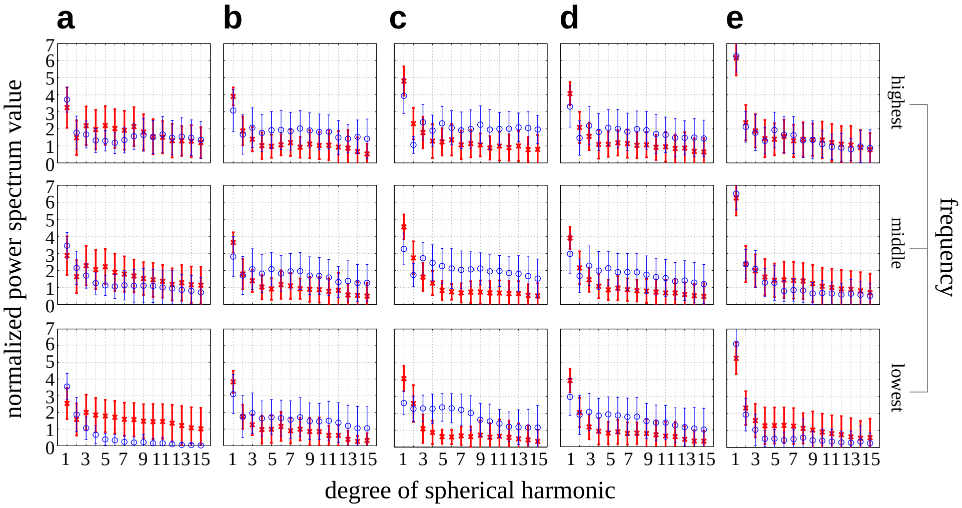

Figure 26: Mean values of normalized power spectra of the populations. a) Rhinolophidae+Hipposideridae pinnae (x) vs. Vespertilionidae pinnae (o). b) Rhinolophidae noseleaves (x) vs. Rhinolophidae pinnae (o). c) Hipposideridae noseleaves (x) vs. Hipposideridae pinnae (o). d) Rhinolophidae+Hipposideridae noseleaves vs. Rhinolophidae+Hipposideridae pinnae (o). e) Rhinolophidae+Hipposideridae noseleaves (x) vs. Phyllostomidae noseleaves (o). Each row represents one beampattern simulation frequency. For the two populations in each group, the mean values of the power spectra and the standard deviations are plotted for the ten simulation frequencies and the 15 spherical harmonic degrees [15].

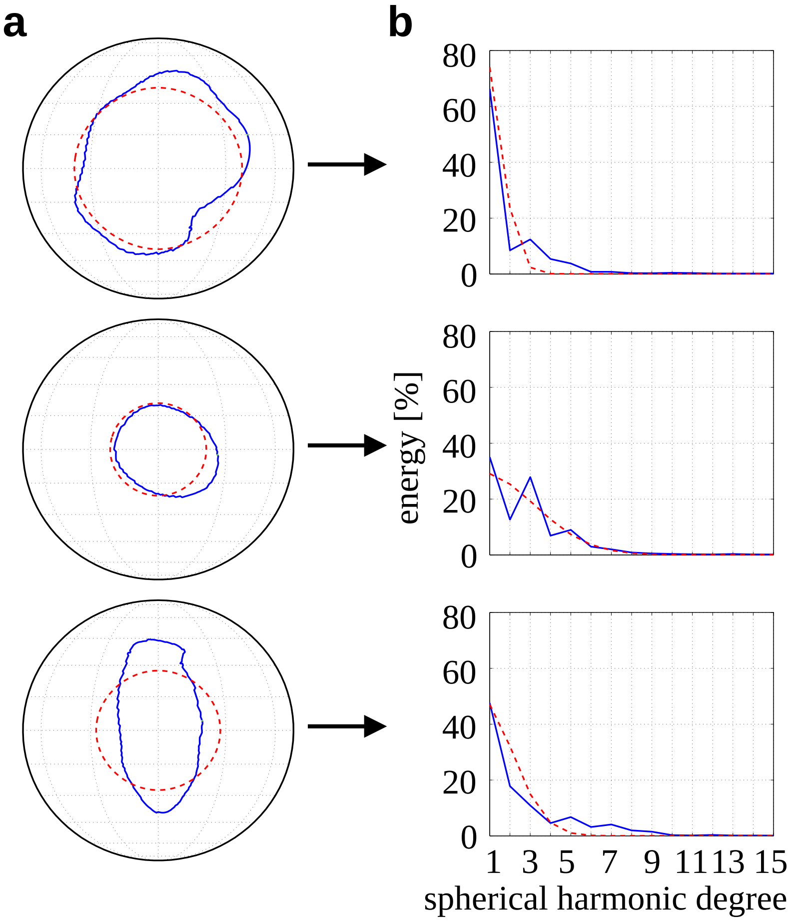

Figure 27: Examples of original beampatterns with heat kernel fits superimposed. a) Cross-section through the numerical beampattern estimates (solid line) together with the fitted heat kernel approximations (dashed line). b) Corresponding power spectra of the numerical beampattern estimates (solid line) with the heat kernel fits (dashed line) [15].

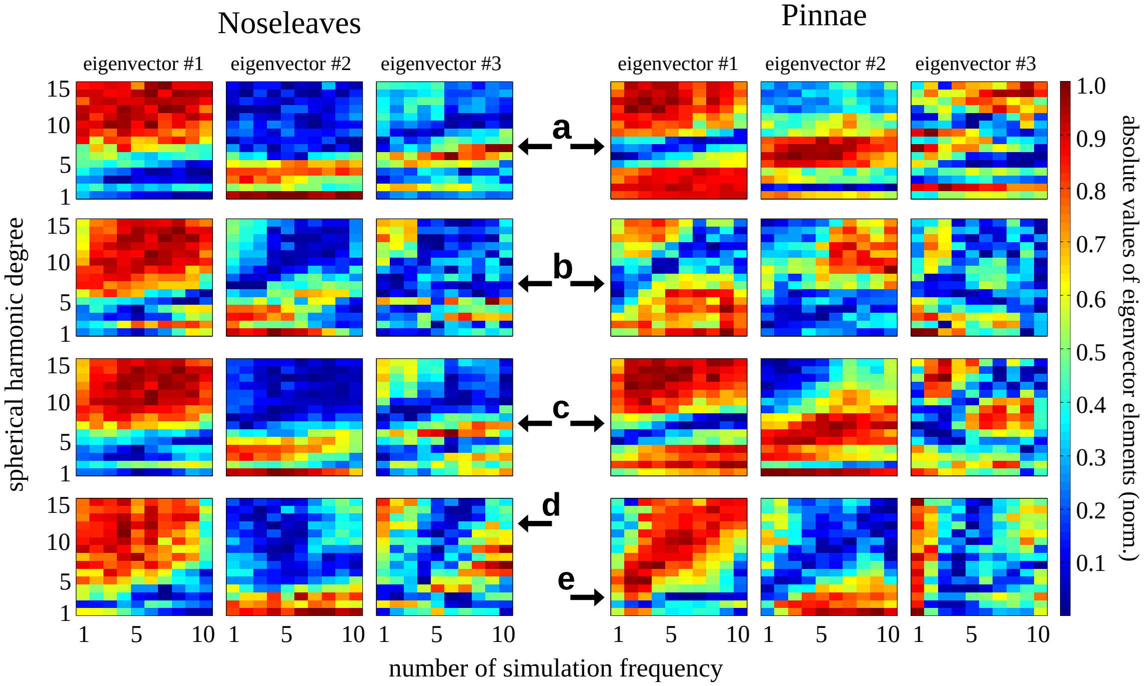

Figure 28: Natural variability of the different populations. a) Rhinolophidae. b) Hipposideridae. c) Rhinolophidae+Hipposideridae. d) Phyllostomidae. e) Vespertilionidae. The images represent the mappings the absolute values of the elements of first three eigenvectors of covariance matrices of the normalized power spectra into the 150-dimensional space of 10 simulation frequencies and 15 spherical harmonic degrees. The absolute values of the elements are linearly encoded by gray scale, where black represents the maximum value [15].

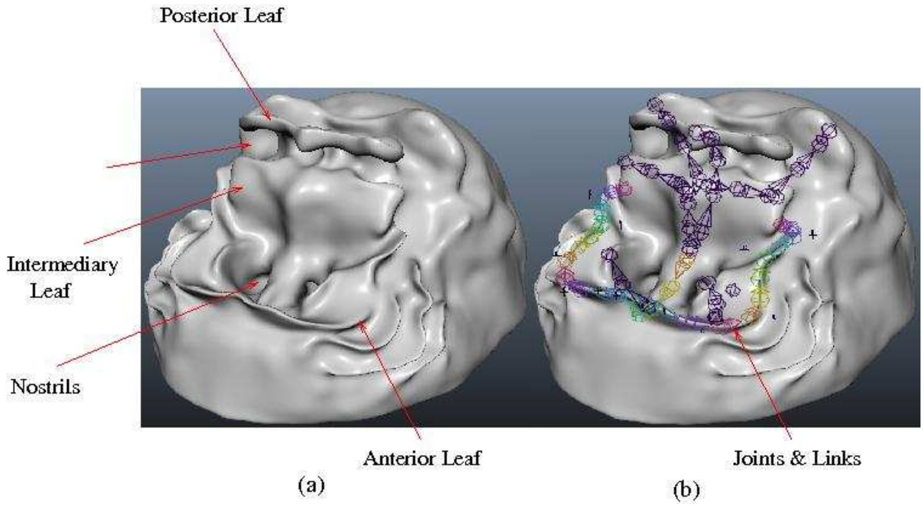

Figure 29: Computer animation techniques used to recreate life-like deformations of the noseleaf shape of a great roundleaf bat (*Hipposideros armiger*): a) noseleaf portions, b) rigging for shape deformations.

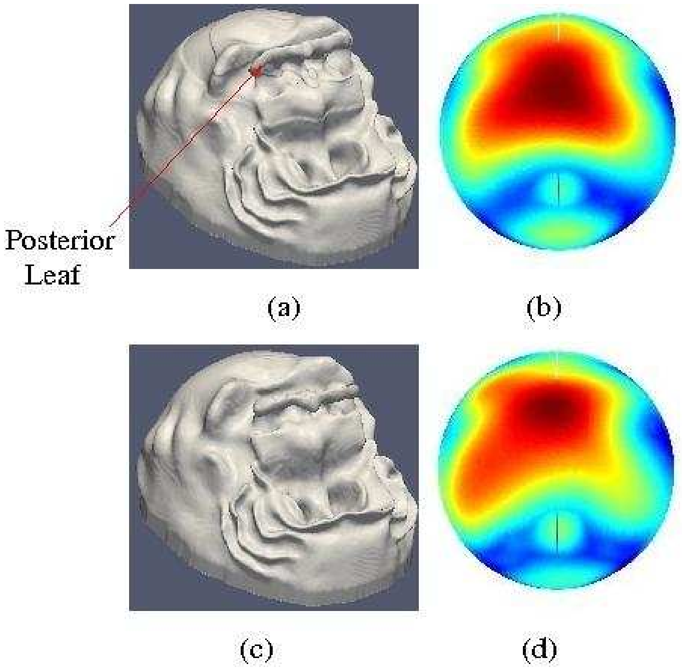

Figure 30: Example of beampattern changes (b,d) in response to changes in the shape of the noseleaf of a great roundleaf bat (*Hipposideros armiger*) (a,c).

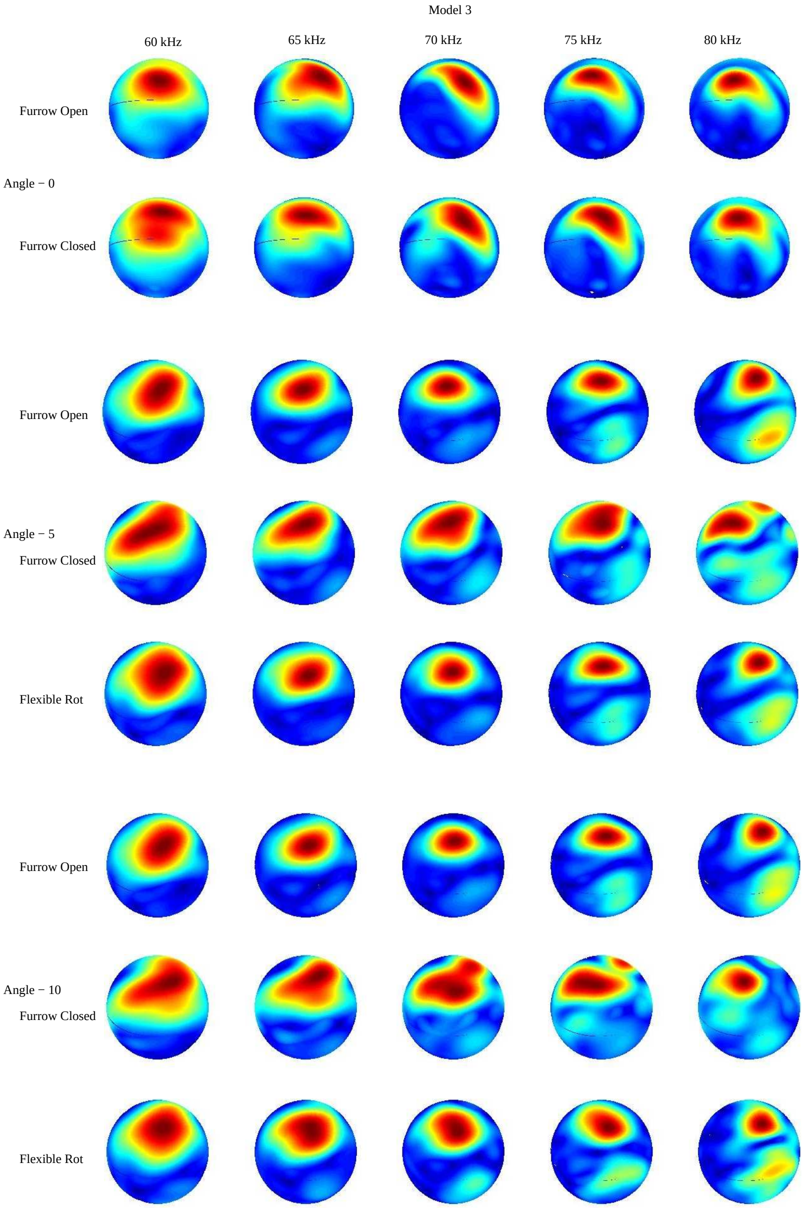

Figure 31: Example of the effects of local shape features on the emission beampattern of the noseleaf of a greater horseshoe bat (*Rhinolophus ferrumequinum*). Beampatterns are shown for different rotation angles of the lancet (0, 5, 10 degrees) and for the natural shape condition (lancet furrows open) and a manipulated shape with closed lancet furrows.

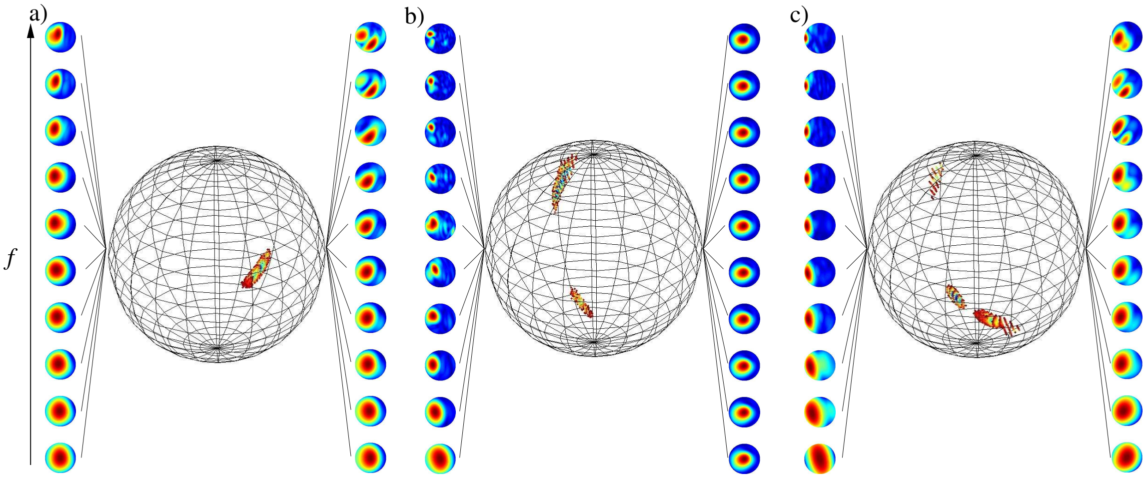

Figure 32: Examples of beampattern alignment based on minimization of a p-norm for the beampatterns from different bat species: a) Asian barbastelle (*Barbastella leucomelas*) and common pipistrelle (*Pipistrellus pipistrellus*), b) long-tongued fruit bat (*Macroglossus sobrinus*) and big-eared horseshoe bat (*Rhinolophus macrotis*), c) Leschenault's rousette (*Rousettus leschenaultii*) and Nathusius' pipistrelle (*Pipistrellus nathusii*). For each comparison, the 10 beampatterns used for the align are shown on the right and the left-hand side and the resulting cost function is visualized in the center. Cost function values are visualized in color (blue represents low) in the vicinity of the minima.